sciendo

Effect of ball milling on hexagonal boron nitride (hBN) and development of Al-hBN nanocomposites by powder metallurgy route

Arka Ghosh[1], Uddeshya Shukla[1], Nityananda Sahoo[1], Sourav Ganguly[2], Pankaj Shrivastava[1], Lailesh Kumar[3,4], Syed Nasimul Alam[1,*]

[1]Department of Metallurgical and Materials Engineering, National Institute of Technology Rourkela, Rourkela, Odisha, Pin-769008, India

[2]Department of Advanced Materials Technology, CSIR-Institute of Minerals and Materials Technology (IMMT), Bhubaneshwar, Odisha, Pin-751003, India

[3]Department of Materials Science and Engineering, Seoul National University, 1 Gwanak-ro, Gwanak-gu, Seoul 08826, South Korea

[4]Pinetree PosMagnesium Co. Ltd., Suncheon-Si, South Korea

This study reports on the exfoliation of bulk hexagonal boron nitride (hBN) by high-energy ball milling and the development of Al-hBN (alumninum-hexagonal boron nitride) nanocomposites by the powder metallurgy (PM) route via the incorporation of the exfoliated hBN in the Al matrix as a nanoreinforcement. The effect of ball milling on the morphology, crystallite size, lattice strain, and thermal stability of hBN powder have also been reported in this paper. Commercially available bulk hBN was ball milled for up to 30 hours in a high-energy planetary ball mill in order to exfoliate the hBN. Although no new phases were formed during milling, which was confirmed by the XRD (x-ray powder diffraction) spectra, ball milling resulted in the attachment of functional groups like hydroxyl (OH) and amino (NH_2) groups on the surface of the hBN, which was confirmed by FTIR (Fourier Transform Infrared Spectroscopy) analysis. HRTEM (high resolution transmission electron microscopy) analysis confirmed the synthesis of hBN having few atomic layers of hBN stacked together after 20 hours of milling. After 20 hours of milling, the hBN particle size was reduced from ~1 μm to ~400 nm, while the crystallite size of the 20-hour-milled hBN powder was found to be ~18 nm. Milling resulted in a flake-like structure in the hBN. Although milling involved both exfoliation as well as reagglomeration of the hBN particles, a significant decrease in the diameter of the hBN particles and their thickness was observed after a long period of milling. The average thickness of the 20-hour-milled hBN flakes was found to be ~32.61 nm. HRTEM analysis showed that the hexagonal structure of the milled hBN powder was maintained. Al-based nanocomposites reinforced with 1%, 2%, 3%, and 5% by weight hBN were fabricated by PM route. The Al-hBN powder mixtures were cold-compacted and sintered at 550°C for 2 hours in argon (Ar) atmosphere. The maximum relative density of ~94.11% was observed in the case of Al-3 wt.% hBN nanocomposite. Al-3 wt.% hBN nanocomposite also showed a significant improvement in hardness and wear resistance compared to the pure Al sample that was developed in a similar fashion. The maximum compressive strength of ~999 MPa was observed in the case of Al-3 wt.% hBN nanocomposite and was approximately twice that of the pure Al sample developed in a similar fashion.

Keywords: *Hexagonal boron nitride (hBN), ball milling, HRTEM, Raman spectroscopy, DSC/TGA, Al-hBN nanocomposites*

1. Introduction

Aluminum (Al) is the second most widely used metal in the world after iron (Fe). It has a low density (2.7 g/cc), good thermal conductivity (237 W/mK), low electrical resistivity (2.65 x 10^{-8} Ω.m), excellent malleability and corrosion resis-

tance, and good formability. Its Young's modulus is 70 GPa, and its Vickers hardness is 160-350 Mpa. The melting point of Al is 660.32°C, and its strength decreases at high temperatures [1–3].

However, there is an increasing demand for Al and its alloys, which have high strength. Al-matrix composites (AMCs) reinforced with suitable reinforcements are being developed to overcome the

* E-mail: nasimulalam@yahoo.com

shortcomings of Al and meet the growing demand for high-strength materials. Strengthening Al with nanofillers like hexagonal boron nitride (hBN) is an excellent option for overcoming the limitations of monolithic Al and could help us achieve a good combination of high strength, stiffness, toughness, and low density.

Since the discovery of graphene, research on other two-dimensional (2D) materials like hBN has attracted considerable interest [4, 5]. hBN is known for its thermal stability, chemical inertness and wide range of applications. It has a low density of 2.3 g/cc and has a very high specific surface area of 0.82-30 m^2/g, and thus it is highly suitable for use as a reinforcement in nanocomposites [6, 7]. hBN has a honeycomb structure of alternate boron (B) and nitrogen (N) atoms bonded by an sp^2 hybridized orbital, forming a strong σ bond. The interlayers are bonded by weak van der Waals forces, allowing them to slide easily between the layers, providing excellent lubricating properties. This is why hBN can provide excellent wear resistance when used as a nanoreinforcement to develop nanocomposites [8–10]. hBN has a very high melting point of 2973°C, which makes it a good high-temperature ceramic, and its thermal conductivity is 550 $Wm^{-1}K^{-1}$. It has a bandgap of 5.9 eV and behaves as an insulator. Its Young's modulus is 800–850 GPa [11–13].

Reinforced materials are of great significance in technological advancements. A lot of research has been done on carbon-based reinforcements, such as carbon nanotubes (CNT), graphene and graphene oxide, and there has been an exponential rise in their industrial applications. On the other hand, one of the major drawbacks of ceramic-based reinforcement materials is their relatively high density.

Due to its excellent properties, hBN has the potential to be used as a reinforcement in composites [14, 15]. Several studies have been reported in the literature on the mechanical and tribological behavior of Al matrix-based composites reinforced with hBN. Firestein et al. [16] observed a dramatic improvement in the mechanical properties of Al composite reinforced with 0.5, 1.5, 3.0, 4.5, 7, and 10 wt.% either boron nitride (BN) microparticles or nanoparticles (BNMPs and BNNPs)

fabricated using the spark plasma sintering (SPS) technique. They reported that composites with 4.5 and 7.0 wt.% of BNMPs showed the highest tensile strengths of 386 MPa at room temperature, whereas at 500°C, the highest tensile strength of 170 MPa was observed in the case of 7 wt.% BNNP reinforced Al-based composite. They also reported that the composites with BNMPs showed a more homogeneous microstructure as compared to the composites developed with BNNPs. This clearly indicates the greater tendency of the nanoparticles to agglomerate compared to the micron sized particles, resulting in better mechanical performance in the case of Al-based composites developed by using BNMPs. They also reported the formation of phases like AlB_2 and AlN during the development of the Al-based composites by SPS.

Khatavkar et al. [17] reported on the tribological properties of AA2024-hBN metal matrix composites developed by the stir casting method. The AA2024 – 0, 3, 6, and 9 wt.% hBN composites were developed by the stir casting process and 1 wt.% magnesium (Mg) was added in order to enhance the wettability of hBN on the surface of the AA2024 alloy. It was reported that the AA2024-hBN composites were lighter than the AA2024 alloy and the density of the composites decreased as their hBN increased. The lowest density was observed in the case of the AA2024 – 9 wt.% hBN composite. They also reported that the Rockwell B hardness of the composites increased with the increase in the content of hBN reinforcement and the hardness of the AA2024 – 9 wt.% hBN composite was 60.66 HBN. The AA2024 – 6 wt.% hBN composite showed the best wear resistance as well as minimum coefficient of wear resistance among all the composites and the AA2024 alloy.

Yonetken and Erol [18] fabricated Al-based composites reinforced with 3, 6, 9, 12, and 15% of BN by conventional microwave sintering at 550°C. They reported the formation of compounds between the Al matrix and the BN reinforcement. Their study showed that the highest microhardness of 42.65 HV was observed in the case of Al at 12% BN, while the highest density of 2.975 g/cc was observed in the case of Al at 3% BN. From their work, they concluded that the best results were observed

in the case of Al 12% BN composite, and as the loading level of BN was increased in the Al matrix, the porosity in the composite increased, resulting in a decrease in hardness.

Loganathan et al. [19] investigated the mechanical properties and wear behavior of AA2024/hBN composites developed by PM route. They developed AA2024 – 0, 2.5, 5, and 7.5 wt.% hBN composites for their study. The composites were sintered at 525°C in Ar atmosphere. Their results revealed that with an increase in hBN reinforcement in the matrix, the hardness, density, and wear resistance of the composite increased significantly. They also reported an improvement in hardness of 68% as compared to that of the pure AA2024 alloy. The AA2024 – 7.5 wt.% hBN composite showed an improvement of 74.9% in wear resistance as compared to the pure AA2024 alloy. This higher wear resistance was due to the formation of lubrication film between the contact zones.

Gostariani et al. [20] developed Al matrix nanocomposites reinforced by 1, 2 and 4 wt.% nano-boron nitride (BN) using a mechanical milling and hot extrusion process and determined their mechanical properties. Mechanical milling was carried out in a planetary ball mill with stearic acid as the process controlling agent (PCA) at 430 rpm for 300 minutes in Ar atmosphere. The milled powder was later annealed at 200°C for 60 minutes and compacted to obtain billets. The billets were then heated at 580°C for 45 minutes and extruded to obtain the final dense billets, which had a diameter of 10 mm. Gostariani et al. reported that a high fraction of the BN nanoparticles dissolved and formed a solid solution in Al matrix during milling, which increased the work hardening rate of the composite powders. Milling resulted in the formation of equiaxed particles and reduction in particle size of Al. By increasing the BN content in the range of 0-4 wt.%, the tensile stress of the hot extruded samples increased from 212 to 333 MPa. The hardness of the nanocomposites having 1, 2, and 4 wt.% hBN was found to increase by 55, 70, and 90% compared to a milled pure Al sample, respectively, and 230, 260, and 300%, respectively, compared to an unmilled pure Al sample. They also reported the formation of in-situ AlN and AlB$_2$ phases by a solid-state reaction with Al during sintering and hot extrusion.

The major objective of the present research work is to improve the mechanical properties and wear behavior of pure Al via the incorporation of hBN nanofiller. Here, hBN nanoplatelets have been synthesized by ball milling bulk hBN in a high-energy planetary ball mill. Bulk hBN can be exfoliated to obtain hBN nanoplatelets that have few layers stacked together by mechanical milling technique. Ball milling is a top-down method for synthesizing nanomaterials and is highly effective in exfoliating 2D materials like hBN and graphene, although the yield in this method is not adequate [21, 22]. The nanostructured milled hBN powder obtained using milling was later added to the Al matrix and mixed by ultrasonication. hBN was used as a nanoreinforcement to investigate the effect of the nanostructured hBN on the various physical and mechanical properties of the Al-hBN nanocomposite.

2. Materials and methods

In the present research work, pure Al powder with a particle size of ~44 μm was procured from Loba Chemie Pvt. Ltd, India, and hexagonal boron nitride (hBN), with a particle size of ~1 μm and 99% purity, was procured from Oxford Lab Fine Chem LLP, India. As shown in Figure 1, the ball milling process was used to exfoliate the pristine hBN and to reduce the number of layers. 10 g of hBN powder was ball milled in a high-energy planetary ball mill at 300 rpm using tungsten carbide (WC) balls and vials, which were coated with cobalt (Co). Milling was done using a ball-to-powder weight ratio of 10:1 using toluene as the process controlling agent (PCA). Ball milling was done for a total period of 30 hours. The samples were collected intermittently after an interval of 5 hours of milling to determine the effect of milling on the milled powder. The crystallite size and lattice strain of the hBN powder before and after milling were determined using the Voigt's method from the XRD diffraction spectra. The Voigt function for the analysis of the integral breadths of broadened x-ray diffraction line pro-
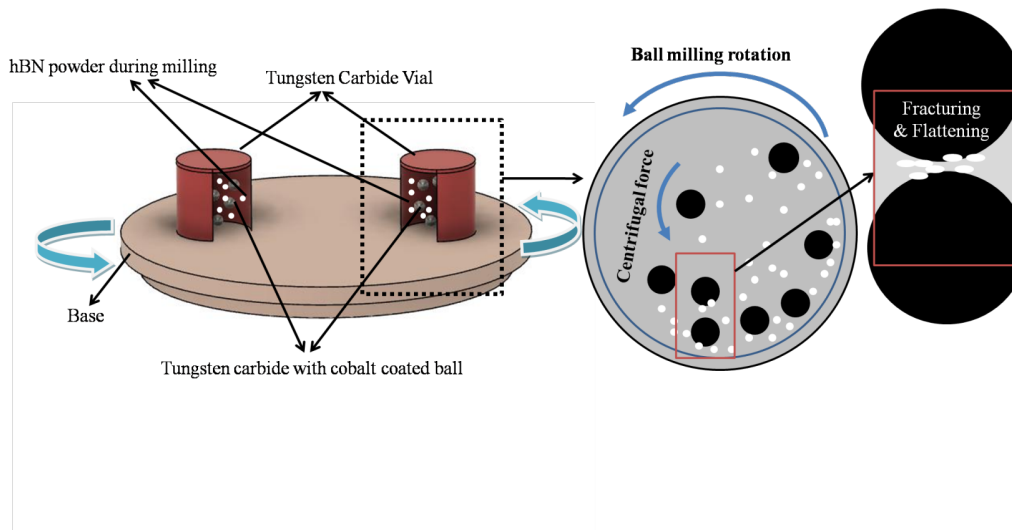
Fig. 1. Ball milling using a high-energy planetary mill

files is a rapid and powerful single-line method for determining the crystallite size and strain. A simple empirical analytical approximation to the Voigt profile is proposed as a weighted sum of the Lorentzian and Gaussian functions. The size- and strain-broadened profiles of the sample typically fit with a pseudo-Voigt function, which is a linear combination of the Gaussian and Lorentzian components. The integral breadth of the Voigt function is expressed through its constituent integral breadths. As the convolution of two Voigt functions is also a Voigt function, the integral breadths are easily separable. The Voigt function has been found to show a superior and satisfactory fit [23–25].

The ball milled hBN powders were characterized using x-ray diffraction (XRD) and scanning electron microscopy (SEM). The XRD analysis of all the powder samples as well as the sintered nanocomposites was done using a Bruker D8 Advance x-ray diffractometer with Co K_α radiation (λ = 1.79026 Å) in the 2θ range from 20°–90°, with a scan rate and step size of about 10°/min and 0.02 respectively. The operating voltage was maintained at 35 kV and the current was 25 mA. The morphology of all the powder samples as well as the sintered samples was analyzed using a Jeol JSM 6480LV scanning electron microscope (SEM) equipped with an INCAPentaFET-x3 x-ray microanalysis system with a high-angle ultra-

thin window detector and a 30 mm^2 Si(Li) crystal for energy-dispersive x-ray spectroscopy (EDXS) analysis. A Supra 55 Zeiss field emission scanning electron microscope (FESEM) was also used for microstructural analysis. The morphology of the milled nanostructured hBN powder was also analyzed using a FEI, Tecnai F30 G2 S-TWIN high resolution transmission electron microscope (HRTEM) with a field emission gun (FEG). The operating voltage of the HRTEM was 300 kV.

The HRTEM analysis of the various hBN powder samples was done using carbon-coated 300 mesh Cu grids. The particle size distribution of both the as-received pristine hBN and the various milled hBN powders was determined using a Malvern Nano Zetasizer particle size analyzer. For the particle size analysis, the various powder samples were ultrasonicated using a probe-sonicator for a period of 3 minutes. Isopropyl alcohol (C_3H_8O) was used as the dispersion medium for the particle size analysis. Raman spectroscopy analysis was done using a WITec Model-XMB3000-3000 PL micro Raman spectrometer equipped with a WITec Alpha300 confocal Raman microscope. The Raman spectra were recorded under ambient conditions using an Ar+ polarized green laser with a wavelength of 532 nm in the range of 40 to 4000 cm^{-1}.

Ultraviolet-visible (UV-Vis) spectroscopy is an

analytical technique that measures the number of discrete wavelengths of UV or visible light that are absorbed or transmitted through a sample in comparison with a reference or blank sample. The UV-Vis spectroscopy was done using a Jasco V-650 double-beam UV-Vis spectrophotometer with a photomultiplier tube (PMT) detector using $BaSO_4$ as a reference in the range of 200–900 nm at room temperature.

Fourier transform infrared spectroscopy (FTIR) was recorded on an IR Pestige-21 Shimadzu spectrophotometer using KBr as the mulling agent. FTIR was done in the spectral range of 600 to 4000 cm^{-1}. The resolution of the infrared rays was maintained at 4 cm^{-1}. The sample scanning as well as background scanning were done 24 times. KBr was used as the carrier for the sample in the IR spectrum, as it has 100% transparency in the range of wave numbers 400-4000 cm^{-1}. Differential scanning colorimetry (DSC) and thermogravimetric analysis (TGA) were done in a Netzsch STA 409C Simultaneous Thermal Analyzer (STA) at a heating rate of 10°C/min in Ar atmosphere to determine the thermal stability of the various samples.

The DSC/TGA analysis was done in the temperature range of 25–1100°C. The procured hBN powder was ball milled for up to 30 hours in order to learn the effect of milling on the structure and morphology of hBN and to synthesize hBN nanoplatelets. The 20-hour-milled hBN powder was then blended with the pure Al powder by ultrasonication in different weight ratios for a period of 2 hour in acetone medium.

A 1000 W ultrasonicator was used in the present research work. The ultrasonicator was equipped with a solid-state ultrasonic generator generating ultrasound in the frequency range of 2 ± 3 KHz and a horn diameter of 12 mm. The process was carried in an acetone medium. Here, acetone $((CH_3)_2CO)$ acted as a process cooling agent and did not react with the solute particles. Acetone also provided uniform dispersion of the nanofiller. A uniform dispersion of the hBN nanofiller in the metal matrix is essential in order to have a good nanofiller-matrix interaction. Good dispersion of the hybrid nanofiller in the Al powder is essential for improved performance of the nanocomposite. In the present work, acetone has been used as the solvent for dispersing the hBN nanofiller and also for blending the hBN nanofiller with the Al metal powder.

The blended powder mixtures were compacted using a uniaxial compaction machine under a load of 550 MPa for a holding time of 5 min. The green compacted pellets were then sintered in a tubular furnace in Ar atmosphere at a temperature of 550°C for 2 h. Al-1, 2, 3, and 5 wt.% hBN sintered nanocomposites were developed using this method. A pure Al sample was also developed with a similar method in order to determine the effect of hBN on the properties of the Al-hBN nanocomposites.

The densities of the sintered samples were determined using Archimedes' principle. Archimedes' principle provides easy and accurate measurement of density, irrespective of the sample shape. The Vickers microhardness of the pure Al sample, as well as the various Al-hBN nanocomposites developed under similar conditions, was determined using a Leco LM248AT microhardness tester with a diamond indentor. The microhardness of the various samples was determined on polished sintered samples under a constant load of 10 gf for a dwell time of 10 s. A ball-on-plate type DUCOM TR 208 M1 wear tester with a 2 mm hardened steel ball indentor (SAE 52100) was used for the wear test of all the sintered samples under a constant load of 15 N for 10 minutes' running time at 20 rpm. The maximum compressive strength and the strain to failure of the various sintered samples were determined by compressive testing of the samples made as per ASTM E9 standard in an Instron Digital Servo electric universal testing machine (UTM).

For analyzing the evolution of the bulk texture of the sintered nanocomposites, a Bruker D8 Advance system with Co-Kα radiation (λ = 1.7909 Å) was used. A Lyneye detector was used to record the data. Five pole figures (111), (200), (220), (222) and (311) were measured. Subsequently, oriented distribution functions (ODFs), a mathematical set of harmonic functions that help in describing texture, were determined using Labotex 3.0. For the texture calculation, no symmetry was applied [26].
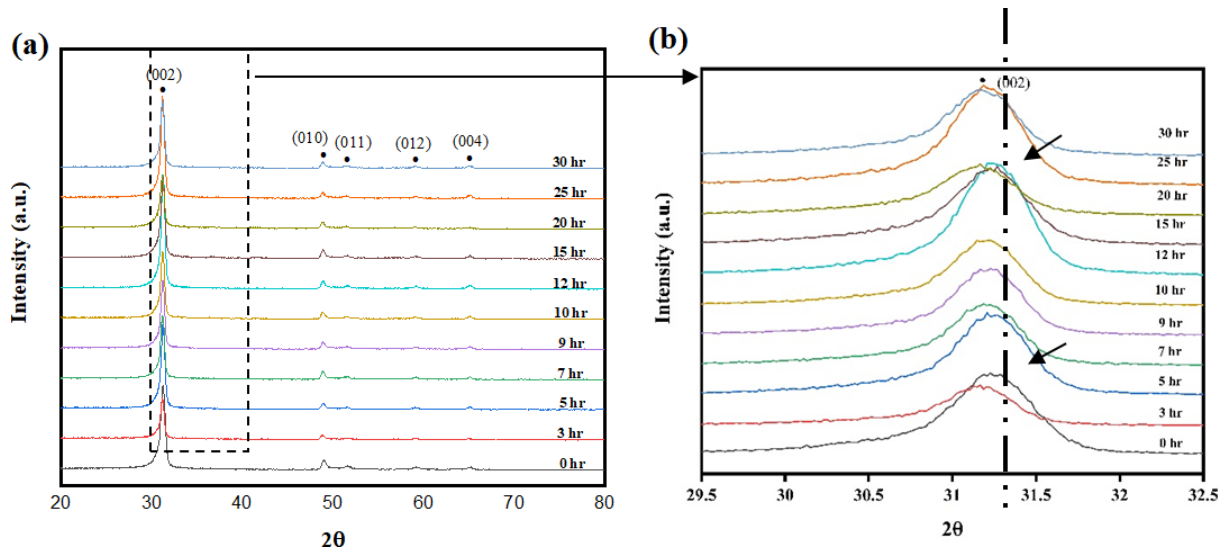
Fig. 2. (a) XRD of hBN powder milled for various periods of time and (b) (002) peak of hBN

3. Results and discussion

The as-received pristine hBN was milled for up to 30 hours in order to determine the effect of milling on the structure and morphology of the hBN and to synthesize hBN nanoplatelets. Samples of hBN were taken out intermittently at intervals of 5 hours. Figure 2(a) shows the XRD spectra of the as-received pristine hBN powder and the various milled hBN powders. XRD peaks corresponding to the (002), (010), (011), (012), and (004) diffraction planes of pristine hBN could be seen at 2θ values of 31.2°, 49.0°, 51.3°, 59.3°, and 65.4°, respectively. The (002) peak corresponding to the basal plane of hBN at 2θ value of 31.27° shows the highest intensity. The d-spacing for the (002) plane calculated using Bragg's law ($\lambda = 2d_{002}Sin\theta$) was found to be 3.32 Å. Considering the (010) plane and using Bragg's law, we get the interplanar d-spacing for the (010) plane (d_{010}) to be 2.16 Å [27, 28]. This clearly indicates high crystallinity in the as-received pristine hBN. However, peak broadening and reduction in intensity of the (002) peak of hBN with milling time is evident, indicating a reduction in crystallite size of hBN with an increase in milling time.

The crystallite size and lattice strain of the hBN powder milled for various periods of time were calculated using Voigt's formula. In this method, the broadening of the peak in the XRD spectrum is considered to be due to both the size and strain effects, and both the size- and strain- broadened profiles were assumed to be Voigtian. For specimen-broadened XRD profiles, Blazar and Ledbetter [29] and Langford [30] later formulated a technique considering both the size and strain effects on the broadening of the peaks using the Voigt function, which is a convolution of the Cauchy-Lorentz distribution and the Gaussian distribution [31, 32].

A slight shift of the (002) peak in the XRD spectra of hBN with the increase in milling time can be seen in Figure 2(b). This is due to the diffusion of trace amounts of O (atomic radius = 0.06 nm) and C (atomic radius = 0.07 nm), which have relatively smaller atomic radii, into the hBN lattice. The diffusion of these impurity atoms with very small atomic radii resulted in the shift of the (002) peak towards higher 2θ values. The EDXS analysis in Figure 4 also clearly indicates the increase in percentage of oxygen in the hBN with increased milling time. The extent of diffusion of impurity atoms into the hBN lattice during milling was very negligible.

Figures 3(a, b) show the variation of the crystallite size and lattice strain of hBN with milling time. From Figure 3(a), it is evident that there is a gradual decrease in the crystallite size of hBN
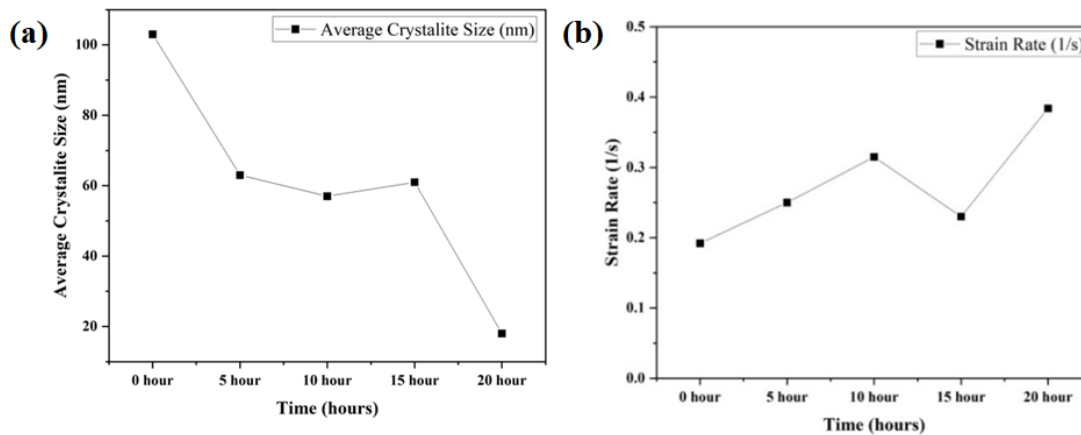
Fig. 3. Variation of (a) crystallite size and (b) lattice strain of hBN with milling time

with an increase in milling time. The decrease in crystallite size is associated with an increase in the lattice strain, as can be seen in Figure 3(b). From Figure 3(a), it is evident that within the period of 5 hours to 15 hours of milling, no significant change in the crystallite size was seen. After 5 hours of milling, there was no significant decrease in the crystallite size of hBN upon further milling up to 15 hours. This is because the reduction in crystallite size due to milling was accompanied by cold welding between the particles. During ball milling, both fragmentation as well as cold welding takes place. A balance of the two processes does not bring about any effective change in the crystallite size. A slight increase in the crystallite size of hBN was observed after 10 hours of milling, followed by a sudden reduction in the crystallite size of hBN beyond 15 hours of milling. The crystallite size of hBN after 15 hours of milling was found to be ~61 nm, showing a sudden reduction to ~18 nm after 20 hours of milling. This was also accompanied by a sudden rise in lattice strain.

Exfoliation of 2D materials like hBN has been done via top-down routes using strong acid or oxidant, ball milling, ultrasonication and hydrothermal techniques. Here, in the present work, exfoliation of the commercially available bulk hBN has been done mechanically by ball milling the bulk hBN powder in a high-energy planetary ball mill for 20 hours. Toluene was used as the process controlling agent (PCA) during milling. The hBN

nanoplatelets obtained after 20 hours of milling, as well as the hBN powder collected intermittently after every 5 hours of milling, have been characterized by several analytical techniques in order to determine the extent of exfoliation achieved with the progress of the milling [33].

Figure 4 shows SEM images of the hBN powder that was milled for various periods of time. After 20 hours of milling, the flat plate-like lamellae of the hBN can be seen in the SEM images in Figures 4(g, h). From the EDXS analysis, along with the SEM images, it is evident that within the initial 5 hours of milling, the milled powder only shows boron (B) and nitrogen (N) in the EDXS analysis, and no other impurities can be seen. However, with the increase in milling time, the oxidation of the milled hBN powder is evident. The EDXS analysis showed no presence of oxygen until after the initial 5 hours of milling. However, beyond 5 hours of milling, oxidation of the hBN takes place. This is evident from the increase in the at.% of O in the EDXS analysis of the 10 hours and 20-hour-milled hBN powders shown, along with the SEM images in Figure 4(f and h), respectively.

Although the at.% of O was not detectable within the initial 10 hours of milling, the at.% of O in the milled hBN continued to increase with the milling time. After 10 hours of milling, the at.% of O in the milled hBN was ~8.95%, and after 20 hours of milling, and the at.% of O in the milled hBN was ~11.91%. After 20 hours of milling, the

Element	At. wt.%
B	33.29
N	66.71

Element	At. wt.%
B	38.58
N	61.42

Element	At. wt.%
B	37.55
N	53.49
O	8.95

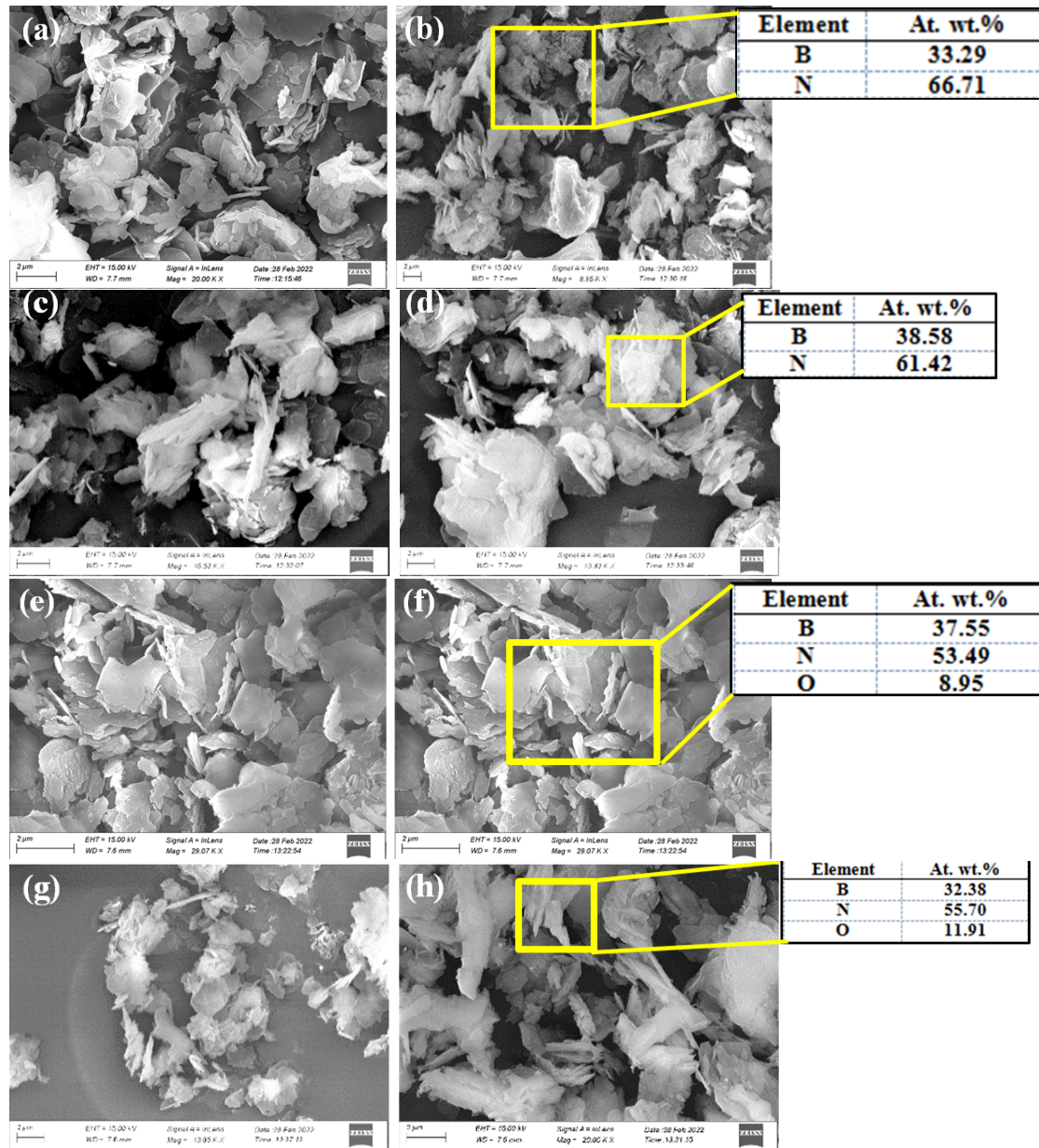| Element	At. wt.%
B	32.38
N	55.70
O	11.91

Fig. 4. SEM micrographs of (a, b) as-received pristine hBN, (c, d) 5-hour-milled hBN, (e, f) 10-hour-milled hBN, and (g, h) 20-hour-milled hBN, along with EDXS analysis

thickness of the flakes had been reduced significantly, indicating clearly that the hBN platelets were successfully exfoliated by milling. The SEM images in Figures 4(g, h) clearly confirm the nanostructured nature of the 20-hour-milled hBN powder and show the polyhedron morphology of the nanoplatelets with a thickness in the range of 150–350 nm.

The DSC curve in Figure 5 provides important information regarding the heat flow, with the temperature rising due to physical and chemical processes like decomposition and oxidation. Thermal analysis of the 30-hour-milled hBN powder was done up to 1100°C at a heating rate of 10°C/min in Ar atmosphere. The DSC plot in Figure 5 shows a sharp peak starting at ~850°C and reaching a maxi-
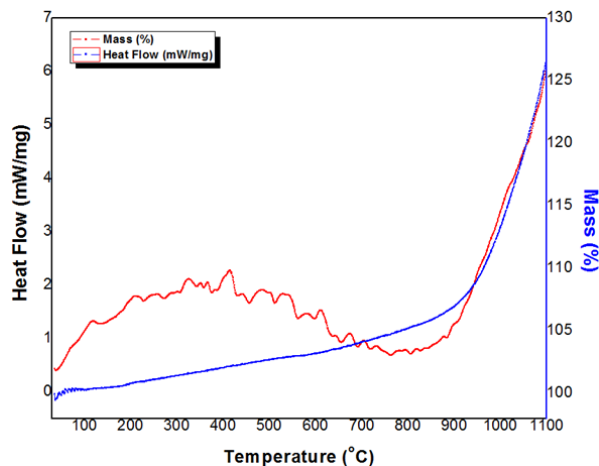
Fig. 5. DSC and TGA plots of 30-hour-milled hBN

mum at ~1100°C. No significant heat flow was observed up to 850°C, but beyond 850°C, the heat flow increased significantly. A sharp rise in the heat flow can be seen in the DSC plot in Figure 5. An intense exothermic peak, related to the oxidation of hBN-forming boron trioxide (B_2O_3), appeared in the range of 850–1100°C. The formation of B_2O_3 was accompanied by a simultaneous increase in mass, as can be seen in the TGA plot given, along with the DSC plot in Figure 5. Initially, the mass almost remained stable and the decomposition and oxidation of hBN nanoplatelets started at ~850°C.

It is clear from the TGA analysis that the hBN has a very high thermal stability and does not show any sign of disintegration up to a temperature of ~850°C. An almost 25% increase in mass was observed due to the formation of B_2O_3. As the hBN powder decomposes, B reacts with O, forming B_2O_3, while N is released as N_2 gas, along with other nitrogen oxides (NO_x) [34–36].

$$2BN + 3/2O_2 \rightarrow B_2O_3 + N_2 \ldots \quad (1)$$
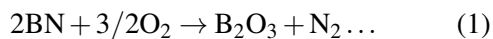
Raman spectroscopy has become an essential technique for characterizing 2D materials like graphene and hBN. The Raman spectra were recorded at room temperature in the spectral range of 400–4000 cm^{-1} using a laser excitation of 532 nm for the as-received pristine hBN powder, as well as for the hBN powder milled for various periods of time. The Raman spectra in Figure 6(a) show a sharp and highly intense G-band centered

at ~1369 cm^{-1} corresponding to the E_{2g} in-plane vibration mode in hBN, which is the characteristic peak of highly pure and crystalline pristine hBN. This is consistent with the position of the G-band in the Raman spectra of hBN, which has been reported in the literature to lie in the range of ~1363–1367 cm^{-1} [37]. No shift in the peak at ~1369 cm^{-1} in the Raman spectra could be seen with milling time (Figure 6(b)). The shift in the peak of the Raman spectrum could have been caused by doping due to the substrate or adsorbates, the heating effect from the laser beam, and strain induced by the substrate. As we do not see any shift in the peak, it can be concluded that none of these significantly affected the hBN powder with the increase in milling time [38].

Figure 6(c) shows the variation of the full width at half maximum (FWHM) of the G-band at ~1369 cm^{-1}. It has been reported that the FWHM of the G-band is directly related to the crystallinity of the hBN nanoplatelets, and a Raman band is narrower in crystalline materials as compared to amorphous materials [39, 40]. As indicated in Figure 6(c), initially a slight reduction in the FWHM of the G-band was observed up to 10 hours of milling, indicating an increase in the crystallinity. The broadening or the decrease in the intensity of the G-band also indicates the extent of the disorder in the sample. A sudden increase in the FWHM was observed in the case of the 15-hour-milled sample due to reagglomeration of the nanoplatelets during milling. However, finally, after 20 hours of milling, the crystallinity was found to be the highest when the FWHM was found to be the lowest, suggesting that the formation of hBN nanoplatelets had few layers of hBN stacked together.

Figure 7 shows the HRTEM images and SAD patterns of the as-received pristine hBN powder and the hBN powder milled for various periods of time. The SAD pattern in Figure 7(d) shows a set of bright spots having sixfold symmetry, which suggests that the as-received pristine hBN powder has a hexagonal structure. The SAD pattern clearly indicates the highly crystalline nature of the as-received pristine hBN. The plate-like structure of the hBN is evident from the HRTEM images of the 10-hour-milled hBN powder in Figures 7(e–
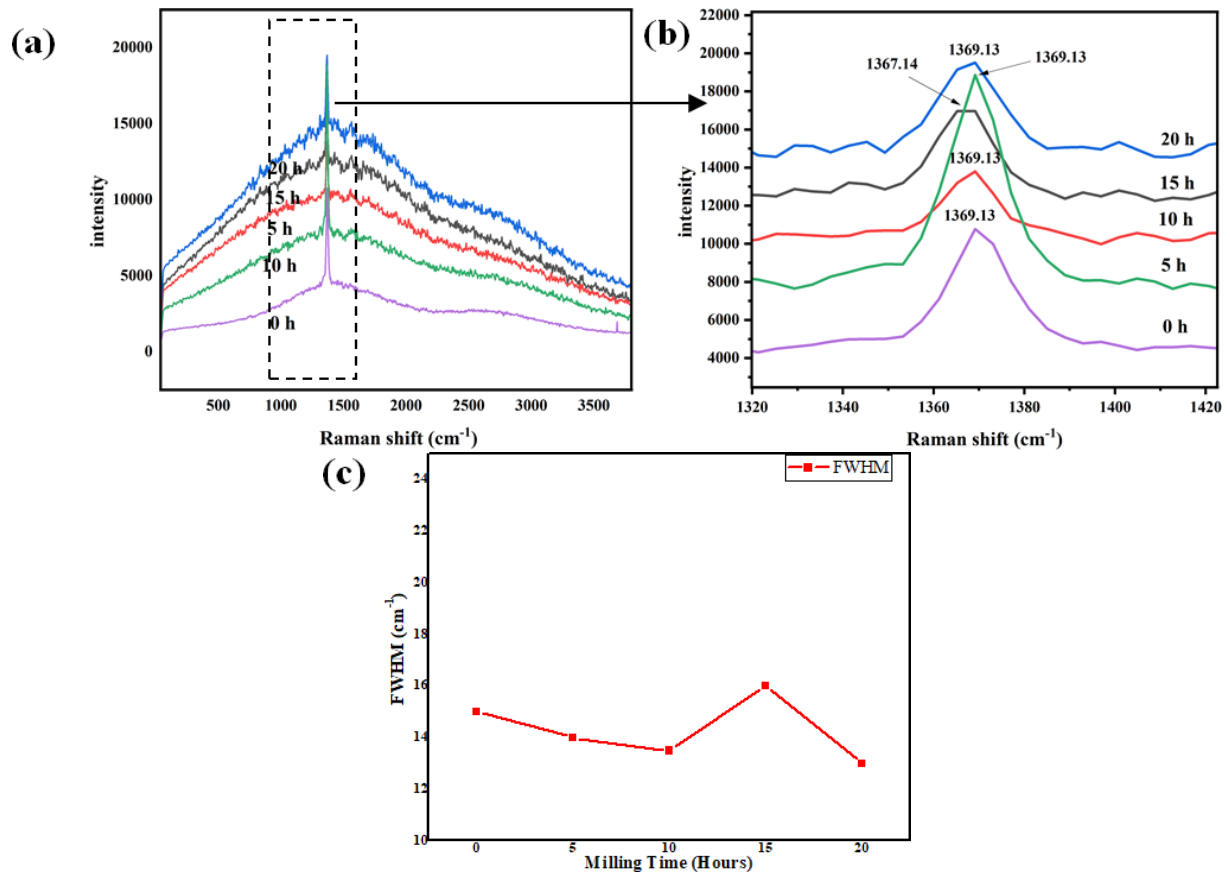
Fig. 6. (a) Raman spectra of hBN milled for different periods of time, (b) peak at ~1396 cm^{-1}, (c) Variation of FWHM at peak of ~1369 cm^{-1} with milling time

g). The HRTEM images of the 10-hour-milled hBN show the multilayered structure of the hBN nanoplatelets, and folding of the hBN nanoplatelets can be seen in Figure 7(f). The SAD pattern in Figure 7(h) shows incomplete rings with bright diffraction spots. The HRTEM images of the 20-hour-milled hBN powder in Figures 7(i–k) clearly indicate that ball milling was successful in exfoliating the hBN powder; the flake-type structure of the 20-hour-milled hBN is very similar to that of graphene. The SAD pattern of the 20-hour-milled hBN powder shows a set of bright dots and several weaker dots with sixfold symmetry, suggesting that the crystalline structure of the hBN powder is preserved even after 20 hours of milling. The rings in the SAD pattern in Figure 7(l) can be indexed to the (002), (014), (010), (012), and (004) diffraction planes of hBN [41, 42].

Figure 8(a) shows the particle size distribution for hBN powder samples milled for various periods of time. It is evident that the particle size ranges from 396.1 to 825 nm for the as-received pristine hBN powder, while the particle size lies in the range of 396.1 to 531.2 nm for 5-hour-milled, 342 to 458.7 nm for 10-hour-milled, 531.2 to 825 nm for 15-hour-milled, and 295.3 to 458.7 nm for 20-hour-milled powder. From this analysis, it can be concluded that with the increase in the milling time up to 10 hours of milling, the particle size decreases, but beyond 10 hours of milling, the particle size increases due to the agglomeration of particles. The 15-hour-milled sample also shows an increase in the particle size. However, the particle size again decreases when milled beyond 15 hours, and a reduction in the particle size can be seen in the 20-hour-milled hBN powder sample as well [43].
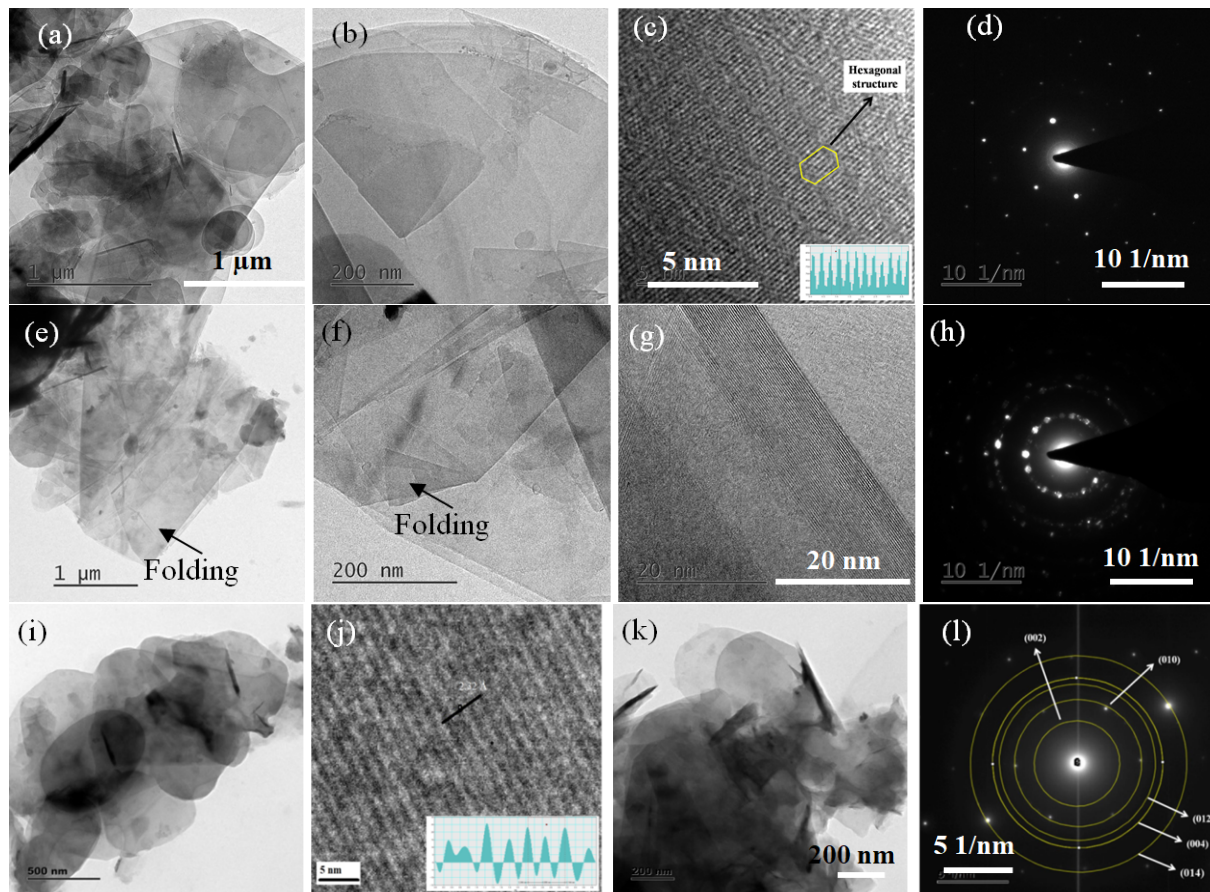
Fig. 7. HRTEM of (a-c) as-received hBN, (e-g) 10 h- (i-k) and 20 h-milled hBN powder. SAD pattern of (d) as-received hBN, (h) 10 h- and (l) 20 h- milled hBN powder
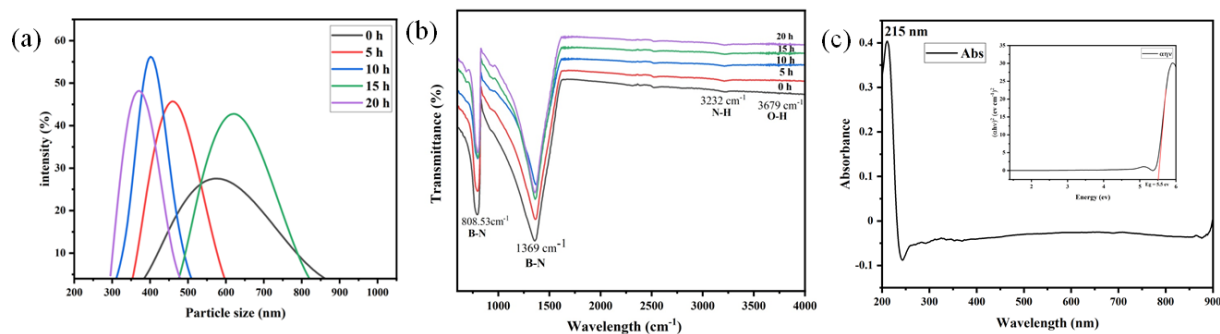

Fig. 8. (a) Particle size distribution, (b) FTIR analysis of hBN milled for various periods of time, and (c) UV-Vis of as-received pristine hBN

Figure 8(b) shows the FTIR transmission spectra of both the as-received pristine hBN powder and hBN powder that has been milled for various periods of time. The FTIR spectra show the characteristic peaks of B-N. Only two characteristically strong and intense peaks, corresponding to the B-N, are seen in the FTIR spectra of the as-received pristine hBN sample and the various milled hBN samples. The low-intensity peaks, corresponding to the other functional groups attached to the hBN, are faint and
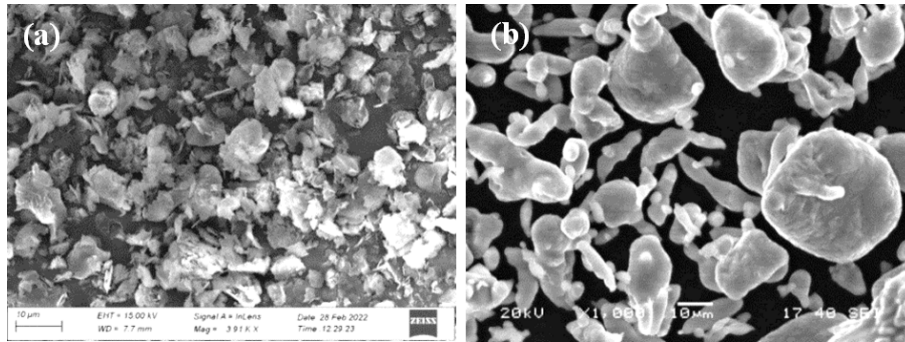
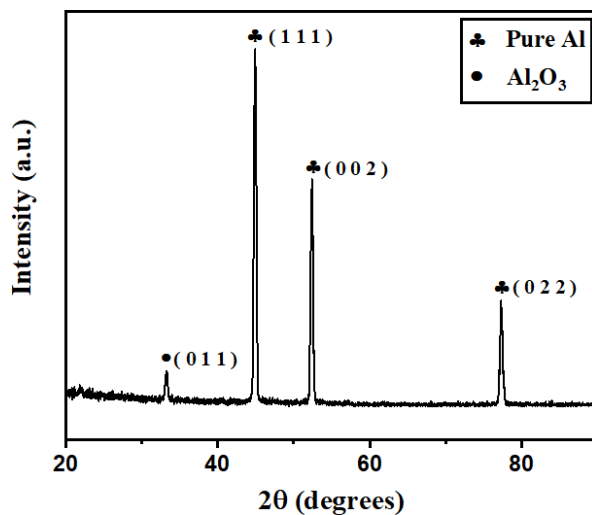Fig. 9. SEM micrograph of (a) 20 h-milled hBN powder (b) pure Al powder

Fig. 10. XRD spectra pure Al

are not clearly visible. The strong and broad peaks are because of the in-plane stretching vibration of the B-N at ~1369 cm^{-1} and out-of-plane bending mode at ~808.53 cm^{-1}. These two peaks represent B-N-B bonds between two hexagonal basal planes and the stretching of the B-N bonds within the basal plane. At ~3232 cm^{-1}, vibrations due to the N-H bond can be seen [44]. At ~3679 cm^{-1}, stretching vibrations due to the O-H bond can be seen.

From Figure 8(b), it can be seen that with the increase in the milling time, the O-H stretching increases, as does the contamination due to oxygen. The vibrations due to the O-H bond are due to absorbed water molecules. Figure 8(c) shows the ultraviolet-visible (UV-Vis) absorption spectrum of the as-received pristine hBN. Tauc plot is used to determine the optical bandgap, or Tauc bandgap, of

semiconductors. Here, the square root of the product of the absorption coefficient and photon energy are plotted against the photon energy. The curve should have a section that is a straight line. If extended to the x-axis, the intercept of this line creates an optical band gap. The figure inset shows the corresponding Tauc plot, which was plotted using Tauc's formula. The optical bandgap range for bulk hBN, as reported in the literature, lies in the range of ~5.2–5.4 eV [45]. The optical band gap for the as-received pristine hBN in the present study was found to be ~5.5 eV. The slight discrepancy of the value found here with the reported theoretical value could be due to the multilayered nature of the hBN. Due to its wide band gap of ~5.5 eV, the hBN behaves as an insulator. The pristine hBN shows high photoluminescence emissions in deep ultraviolet range of 200–220 nm. An intense luminescence peak is seen at around ~215 nm.

Apart from analyzing the effect of milling on the as-received pristine hBN powder, Al-hBN nanocomposites were also developed by powder metallurgy (PM) route. Figures 9(a, b) show SEM micrographs of 20-hour-milled hBN powder and pure Al powder, respectively. The 20-hour-milled hBN powder was blended with the Al powder to prepare the Al - 1, 2, 3, and 5 wt.% hBN powder mixtures. The SEM image in Figure 9(a) shows the hBN nanoplatelets with an average particle size in the range of ~10–12 µm. Al particles having different sizes can be seen in the SEM micrograph of pure Al powder in Figure 9(b). The SEM image of Al powder in Figure 9(b) shows dumbbell-shaped Al particles with sizes in the range of ~35–100 µm.
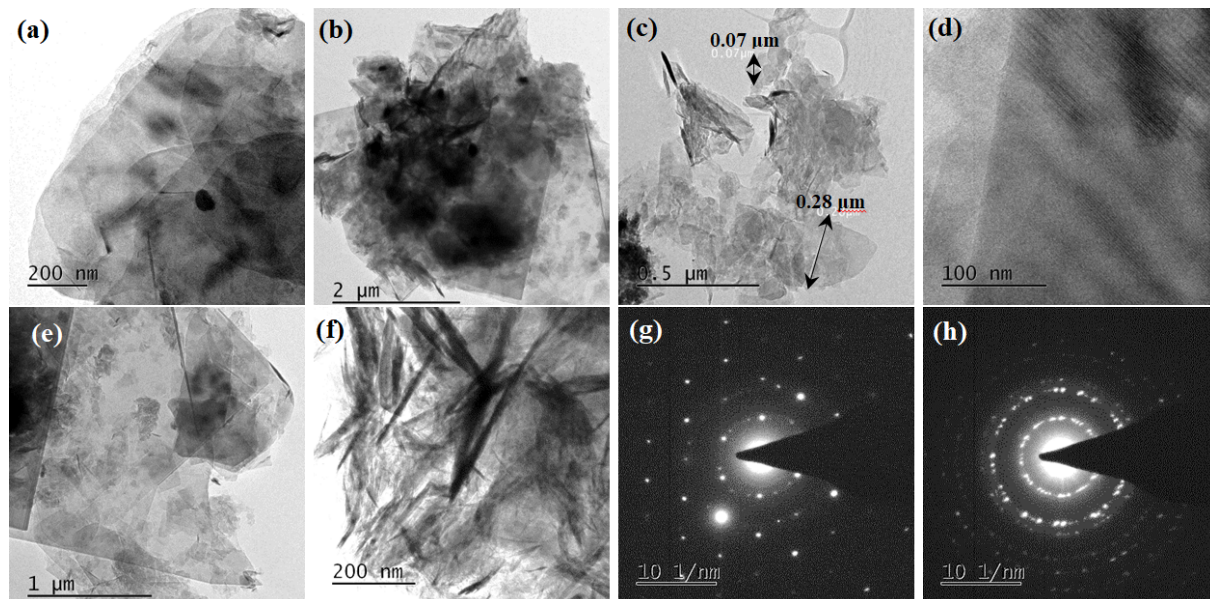
Fig. 11. (a–f) HRTEM images and (g, h) SAD patterns of Al-3 wt.% hBN powder mixture

Figure 10 shows the XRD spectra of the pure Al powder. The XRD spectrum of pure Al powder shows (011), (111), (002), and (022) diffraction peaks corresponding to various planes of FCC Al. In the XRD plot in Figure 10, a peak corresponding to the (011) plane of aluminum oxide (Al_2O_3) can also be seen due to the oxidation of the Al powder when its surfaces were exposed to the open atmosphere.

A thin hard layer of Al_2O_3 also developed on the Al surface due to the oxygen in the air. Due to the strong affinity of Al towards oxygen, Al is readily oxidized by the atmospheric oxygen and a thin passivation layer of Al_2O_3 quickly forms on the exposed Al surface. This layer protects the Al from further oxidation. The presence of the Al_2O_3 layer on the Al particles could affect the wettability of the hBN on the surface of the Al particles during the development of Al-hBN nanocomposites [46].

Figure 11 shows the HRTEM images and SAD patterns of the Al-3 wt.% hBN powder mixture. The Al and hBN powders were blended by ultrasonication in acetone medium for 2 hours. Dark Al particles can be seen trapped within the hBN flakes. A good mixing between the Al particles and the hBN flakes can be seen. From the HRTEM micrographs, close association between the Al particles and the hBN flakes can be observed and the Al particles and the hBN flakes are found to be in contact with each other [47, 48].

The SAD pattern in Figure 11(g), which was obtained from the hBN flakes in the Al-3 wt.% hBN powder mixture, shows a well-defined hexagonal diffraction spot pattern indicating six-fold symmetry of the hexagonal structure of the hBN. The SAD pattern indicates that the hBN has a high degree of crystallinity and that the structure of the hBN is preserved during the blending of the Al and the hBN powder by ultrasonication. Such a spot pattern, instead of a ring pattern, indicates that the hBN flakes contain randomly oriented domains and that the hBN consists of randomly stacked few layers of hBN assembled over one another. The SAD pattern in Figure 11(h) shows sharp, incomplete concentric diffraction rings along with bright diffraction spots, which correspond to the different diffraction planes of polycrystalline FCC Al.

Figure 12(a) shows the XRD spectra of sintered Al-hBN with different wt.% nanocomposites. A low- intensity peak corresponding to the (002) diffraction plane of hBN can be observed at the 2θ value of ~32°. The low intensity of the (002) peaks of hBN is due to the low loading level of hBN reinforcement in the Al matrix. The XRD spectra
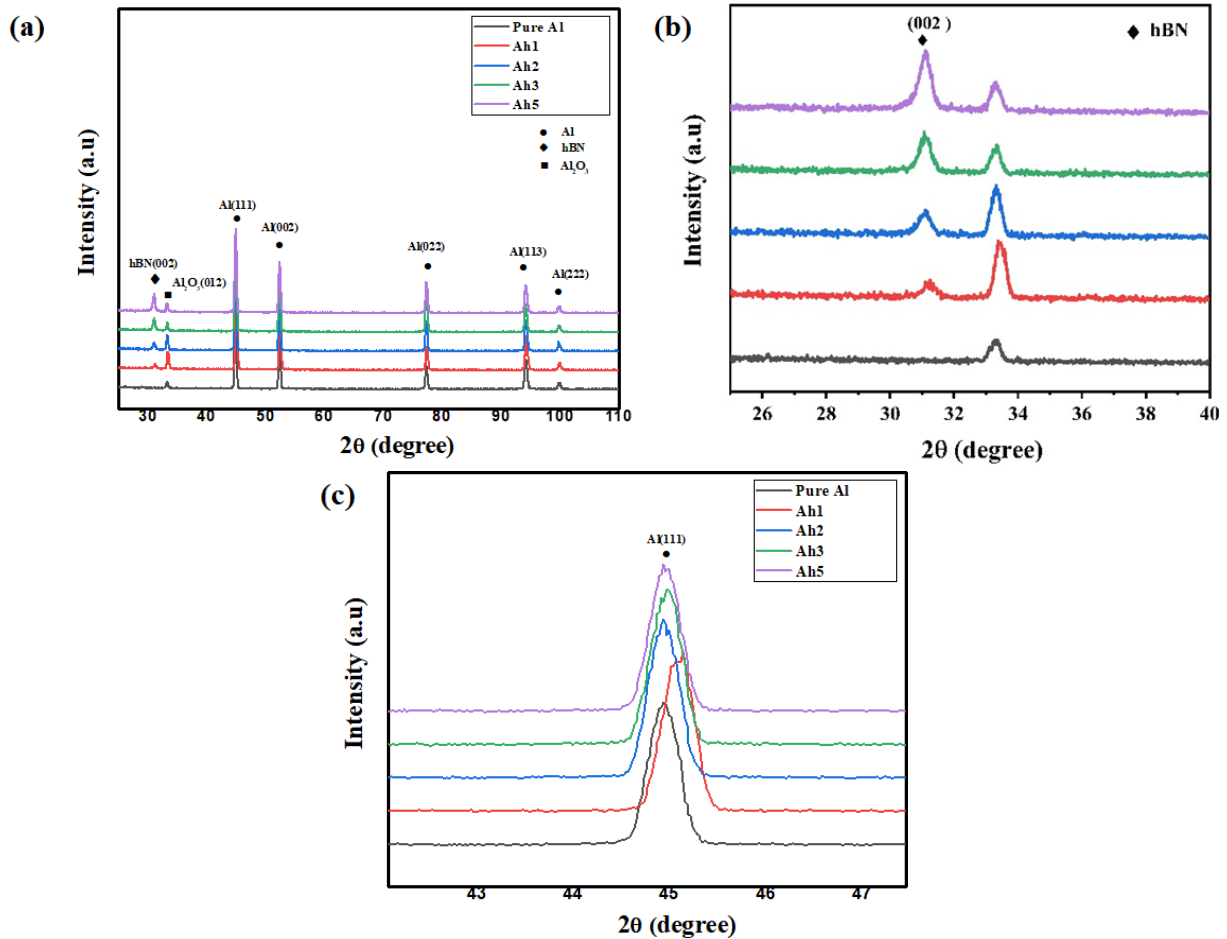
Fig. 12. (a) XRD of sintered pure Al and Al-hBN nanocomposites, (b) (002) peak of hBN, (c) (111) peak of Al

also show peaks corresponding to the (111), (002), (022), and (113) diffraction planes of Al at 2θ values of $45.0°$, $52.4°$, $77.4°$, and $94.3°$. From Figure 12(b), it is evident that with the increased loading level of the hBN nanofiller in the Al matrix, there is an increase in the intensity of the (002) peak of hBN. The highest intensity of the (002) peak of hBN was seen in the case of Ah5 (Al-5 wt.% hBN) nanocomposite at 2θ value of ~$31.16°$.

Figure 12(c) shows the shift in the Al(111) peak in the various Al-hBN nanocomposites. A slightly higher shift in the Al(111) peak could be seen towards the higher 2θ values in the case of Al-1 wt.% hBN nanocomposite, as compared to the Al-2, 3 and 5 wt.% hBN nanocomposites. The shift in the Al(111) peak towards the higher 2θ values is due to the diffusion of small impurity atoms

like O (atomic radius = 0.06 nm), B (atomic radius = 0.085 nm), N (atomic radius = 0.065 nm), and C (atomic radius = 0.07 nm) into the Al lattice (atomic radius = 0.143 nm) at the high processing temperature of 550°C. The lower loading level of the hBN nanofiller was found to be favorable for the diffusion of these impurity atoms with small atomic radii into the Al lattice. The diffusion of small impurity atoms was restricted by a higher loading level of the hBN nanofiller in the Al-hBN nanocomposites.

It should be noted that the wettability of hBN on the surface of the Al particles can be significantly impacted by this oxide layer. Al_2O_3 has a propensity to attract and bind with water molecules, making it a relatively hydrophilic substance. The hydrophobicity of hBN means that it has a propensity
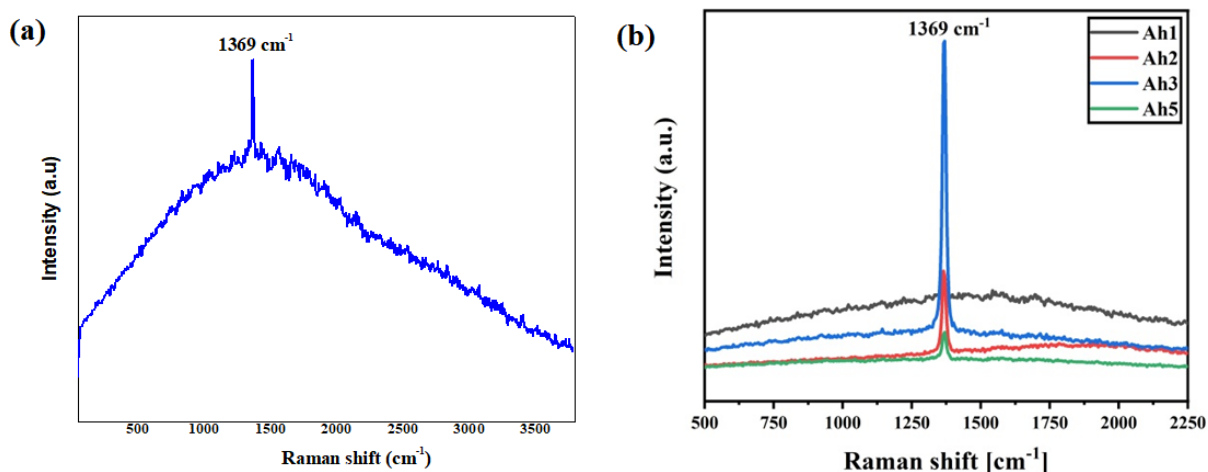
Fig. 13. Raman spectrum of (a) pure hBN powder and (b) sintered Al-hBN nanocomposites
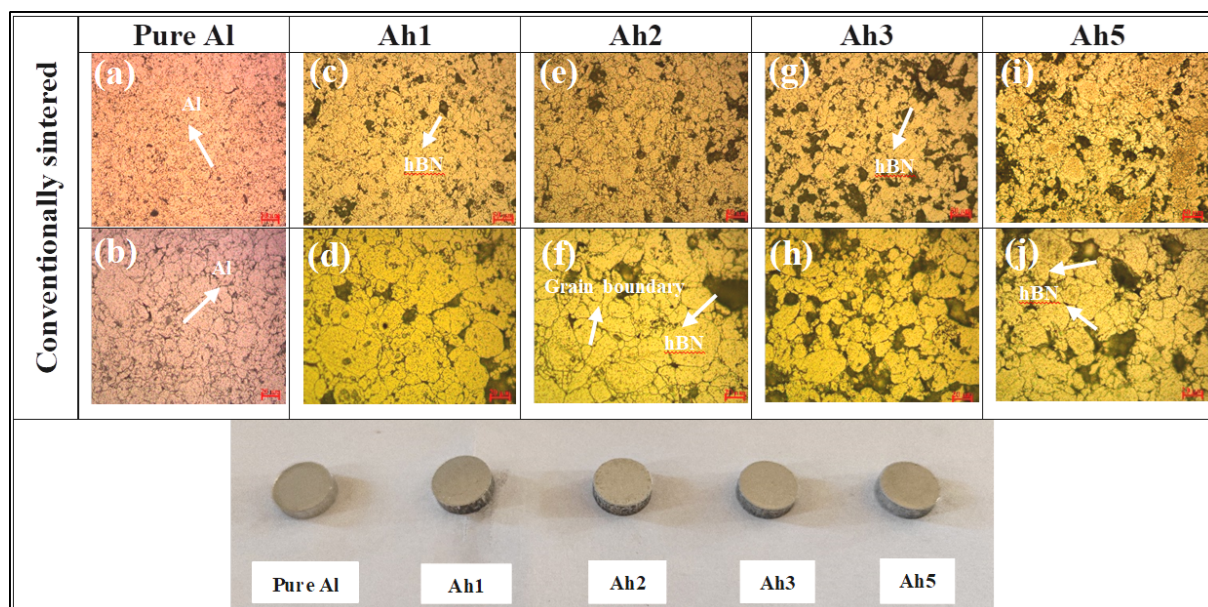

Fig. 14. Optical micrographs of (a, b) pure Al, (c, d) Ah-1, (e, f) Ah-2, (g, h) Ah-3, and (i, j) Ah-5 nanocomposites

to resist water and other polar molecules, which can make it challenging to create strong binding with an Al surface that is covered by a layer of Al_2O_3. Hydrophobic materials such as hBN may find the surface of Al_2O_3 less favorable. Therefore, the existence of the Al_2O_3 layer may provide a barrier that could prevent the adherence of hBN particles to the Al surface, which could result in poor hBN wettability on the Al surface. This can impair hBN dispersion in the Al matrix and degrade the me-

chanical characteristics of the Al-hBN nanocomposites.

Figure 13 shows the Raman spectrum of as-received pure hBN powder Al-3 wt.% hBN nanocomposite. The Raman spectrum of the various Al-hBN nanocomposites in Figure 13(b) shows a sharp and intense peak at ~1370 cm^{-1} corresponding to the in-plane E_{2g} mode or the G-band of the hBN [49]. The sharp and intense peak at ~1370 cm^{-1} in the Raman spectra of all the Al-
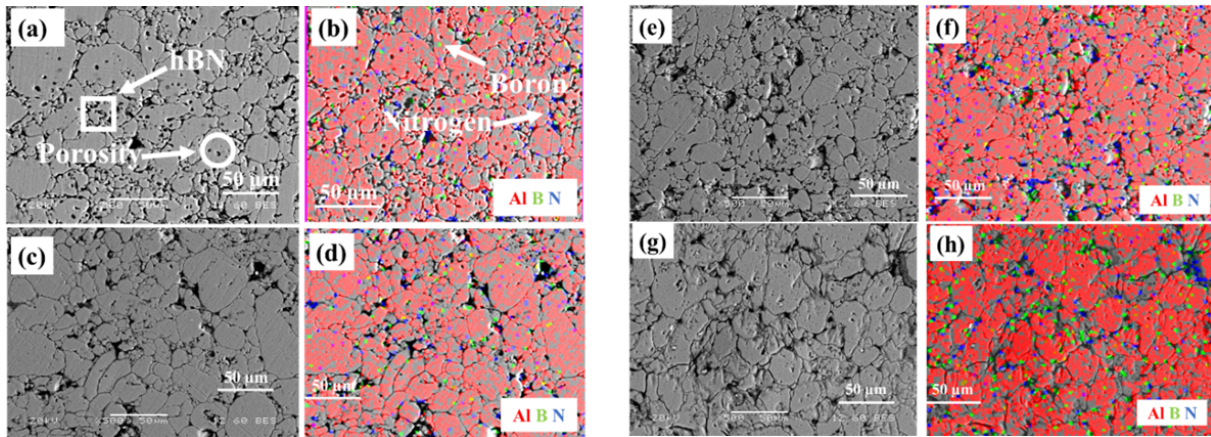
Fig. 15. (a, c, e, g) SEM images and (b, d, f, h) Elemental mapping of Ah-1, Ah-2, Ah-3, and Ah-5 nanocomposites, respectively

hBN nanocomposites suggests a highly crystalline nature in the hBN nanofiller in the various Al-hBN nanocomposites. Therefore, it can be concluded that the structural integrity of the hBN nanofiller incorporated into the Al matrix is preserved, even after sintering at 550°C for 2 h. It should be noted that hBN has a high thermal stability of up to ~850°C, as is evident from the DSC/TGA plot in Figure 5.

Figure 14 shows the optical micrographs of sintered pure Al sample and the various Al-hBN nanocomposites. From the optical micrographs, it is evident that up to the loading level of 3 wt.% hBN in the Al matrix, the distribution of the hBN in the Al matrix is uniform. The optical micrographs revealed the grain refinement of the Al matrix, which occurred due to uniform distribution of the nanoreinforcement at lower loading levels. This very effectively improved the mechanical and tribological performances of the nanocomposites. However, an increase in the loading level of the hBN nanofiller in the Al matrix resulted in the agglomeration of the nanofiller in the Al matrix. A strengthening in the nanocomposites takes place via the Orowan strengthening mechanism [50, 51].

Figure 15 shows the SEM images of the Ah1, Ah2, Ah3, and Ah5 nanocomposites, along with their elemental maps. The SEM images of the nanocomposites in Figures 15(a, c, e, and g) show a highly dense microstructure in the nanocomposites, with no large pores visible. As the sintering was

done at 550°C for 2 hours in Ar atmosphere, which is very close to the melting point of Al (660.3°C), solid-state sintering had taken place. The SEM images clearly indicate good densification to have taken place at this sintering temperature. The elemental maps clearly display the uniform dispersion of the hBN nanofiller in Al matrix up to the loading level of 3 wt.% of hBN nanofiller in the Al matrix. With the gradual increase in the loading level of the hBN nanofiller in the Al matrix an increase in the size of the hBN agglomerates at the Al grain boundaries could be seen. Increasing the hBN nanofiller content beyond 3 wt.% resulted in the formation of hBN clusters in the Al matrix [52, 53]. No interfacial product at the grain boundaries of the Al matrix and the hBN nanofiller could be seen. From the elemental maps of Al, B, and N in Figures 15(b, d, f, and h), it is evident that the hBN nanofillers are mainly found at the grain boundaries of the Al matrix. With the increase in the loading level of the hBN, nanofiller agglomerates of hBN can be seen at the grain boundaries (Figure 15(h)).

The combined plot of relative density and theoretical density is presented in Figure 16(a). The relative density of the pure Al sample was found to be ~88.14%. Maximum densification was achieved at a loading level of 3 wt.% of the hBN nanofiller in the Al matrix. Among all the Al-hBN nanocomposites, the maximum relative density of ~94.11%
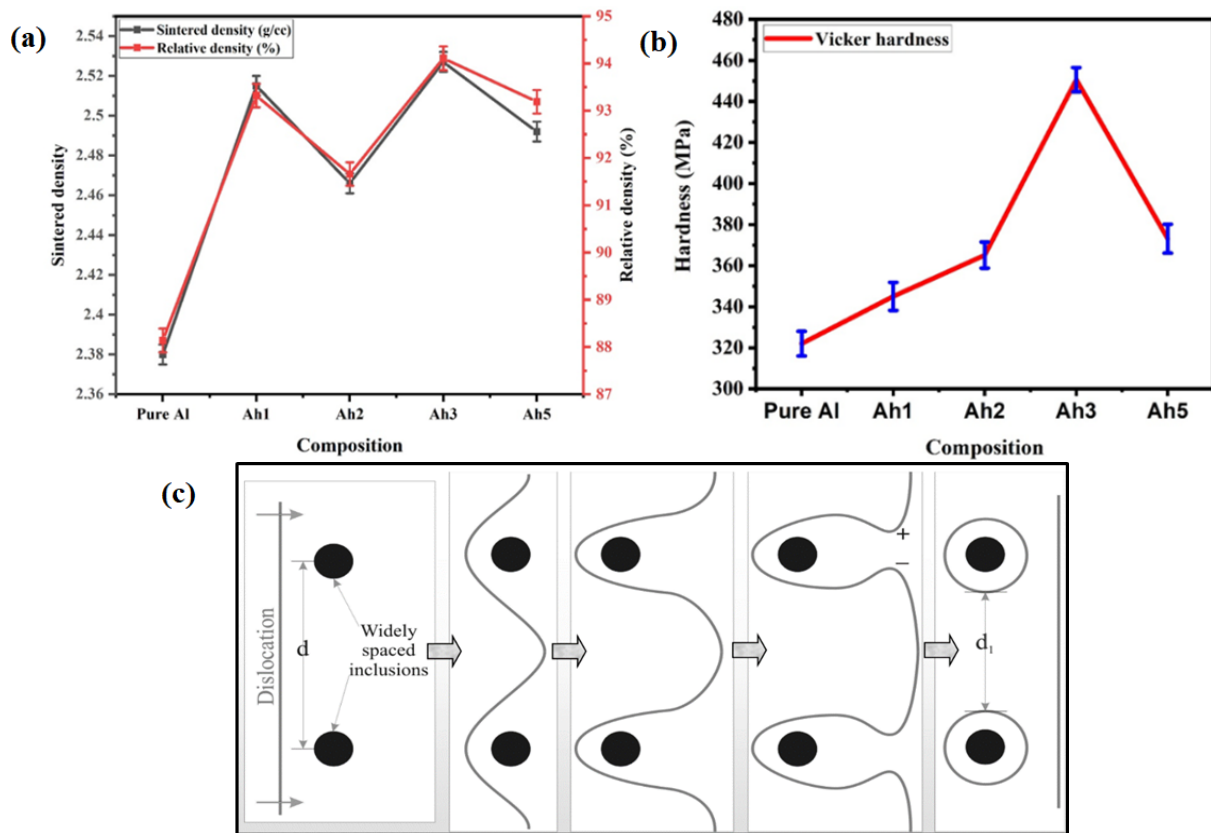
Fig. 16. (a) Relative density and sintered density of sintered pure Al and various Al-hBN nanocomposites, (b) Vickers hardness of the pure Al and various nanocomposites, and (c) Schematic diagram of the Orowan bowing mechanism

was achieved in the case of the Al-3 wt.% hBN nanocomposite. Further addition of hBN nanofiller in the Al matrix resulted in lower relative density of the Al-hBN nanocomposite. In the case of Al-5 wt.% hBN nanocomposite, the relative density was found to be ~93.19%.

Figure 16(b) shows the variation in hardness of the Al-hBN nanocomposites with the increase in their hBN content. The plot shows that the hardness of all the Al-hBN nanocomposites is higher than the pure Al sample developed similarly. At lower loading level, because of the uniform distribution of nanofiller, interfacial distances between the particles decrease, resulting in enhancement in mechanical properties like hardness. The maximum hardness of ~450 MPa was achieved in the case of Al-3 wt.% hBN (Ah-3) nanocomposite. The hardness of the Ah3 nanocomposite is ~40%

higher than the pure Al sample (~322 MPa) developed under similar conditions. The addition of hBN nanoreinforcement in the Al matrix is responsible for the improvement in hardness because it provides a strengthening effect within the Al matrix. However, the addition of this nanoreinforcement beyond 3 wt.% gradually decreased the hardness of the nanocomposite due to the agglomeration of hBN in the Al matrix at higher loading levels. At lower loading levels of the nanoreinforcement, the uniform distribution of nanoreinforcement takes place, which reduces particle interface lengths, resulting in the increase in mechanical properties like strength and hardness of the nanocomposites [54, 55].

The improvement in the hardness of the nanocomposites is due to the Orowan strengthening mechanism. Orowan strengthening is caused
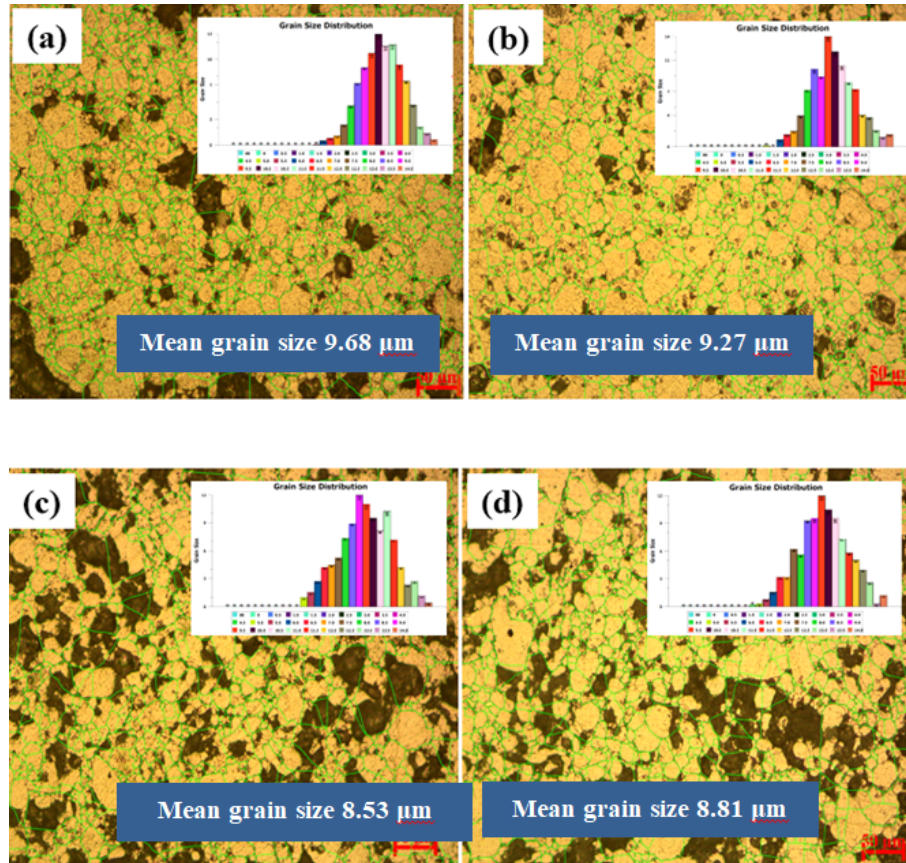
Fig. 17. Optical micrographs of the (a) Ah1, (b) Ah2, (c) Ah3, and (d) Ah5 nanocomposites and grain size distribution of Al

by the resistance of closely spaced hard particles to the passing of dislocations and is very important for Al-based nanocomposites. Figure 16(c) is a schematic diagram explaining the Orowan mechanism [56, 57]. From Figure 17, it is evident that the grain size of Al is minimal in the case of the Ah3 nanocomposite. In this nanocomposite, the Al was reinforced with 3 wt.% hBN, which resulted in a uniform distribution of the nanofiller in the Al matrix without the formation of any large-sized agglomerates. Due to the uniform distribution of the hBN nanofiller, no abnormal grain growth in the Al matrix was seen. The uniform distribution of the hBN nanofiller at the grain boundaries of the Al matrix restricted the grain growth, resulting in more uniform fine-sized grains in the Al matrix. This also led to higher relative density of the Ah3 nanocomposite, and also better hardness, wear properties and compressive strength in the

nanocomposites.

Figures 18(a–c) are HRTEM images of the Ah1 sample having a loading level of 1 wt.% hBN in the Al matrix. Dislocations can be seen the Al matrix, along with dark-colored regions at the Al grain boundaries corresponding to the hBN nanofiller. The hBN nanofillers are mainly found at the Al grain boundaries. The SAD pattern in Figure 18(d) shows sharp concentric rings corresponding to the polycrystalline Al matrix. Similar HRTEM images are also seen in Figures 18(e–g) of the Ah3 sample having a loading level of 3 wt.% hBN in the Al matrix. In the HRTEM image in Figure 18(g), hBN can be clearly seen agglomerated at the Al grain boundary. The SAD pattern in Figure 18(h) shows bright spots corresponding to the hBN nanofiller. Dislocations can also be seen in the Al matrix in the HRTEM images in Figures 18(e–g). The dark spots in the Al grains are Al_2O_3 nanoparticles formed
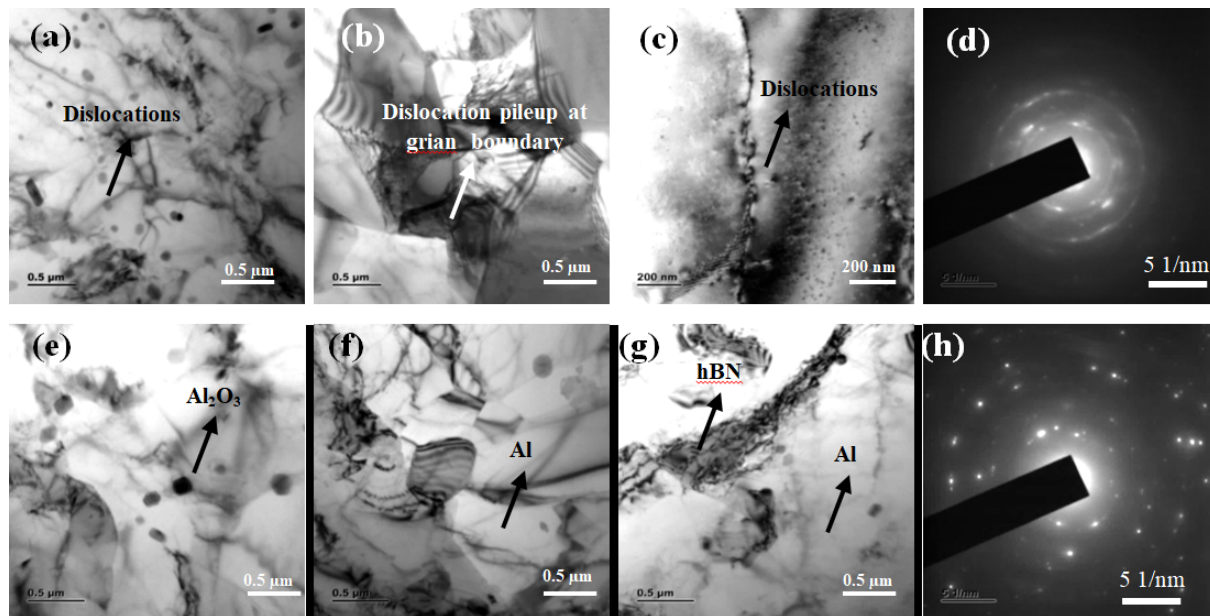
Fig. 18. (a–c) HRTEM micrographs, and (d) SAD pattern of Ah1 nanocomposite, (e-g) HRTEM micrographs, and (h) SAD pattern of Ah3 nanocomposite

due to the oxidation of the Al during sintering. Although sintering was done in Ar atmosphere, Al was oxidized due to the residual oxygen in the Ar gas. The oxidation the Al matrix was also confirmed by XRD analysis (Figure 12).

The influence of the addition of hBN nanoreinforcement on the wear behavior of the Al-hBN nanocomposites was also analyzed. A dry-sliding wear test was conducted on the sintered pure Al and all the Al-hBN nanocomposites using a ball-on-plate tribometer. Wear depth against time and wear rate and mass loss against time of the Al-hBN nanocomposites are plotted in Figures 19(a, b), respectively.

From Figure 19(b), it is evident that the wear rates of all the Al-hBN nanocomposites was lower than that of the pure Al sample developed in similar conditions. The reduced wear rate of the nanocomposites can be attributed to the lubricating effect of the hBN nanofiller [58, 59]. The wear results show that as the hBN content was increased from 1 wt.% to 3 wt.% in the Al matrix, the wear resistance of the Al-hBN nanocomposites also showed a gradual increase (Figure 19(b)). Beyond the 3 wt.% loading level of the nanofiller, the wear resistance of the

Al-hBN nanocomposites showed a decrease. This trend in the variation of the wear behavior of the nanocomposites was very similar to the trend in the variation of the hardness of the nanocomposites. This is due to the uniform distribution of the hBN nanofiller within the Al matrix at lower loading levels of the nanofiller. As the loading level of the nanofiller in the Al matrix was increased beyond 3 wt.%, it resulted in the agglomeration of the nanofiller, which adversely affected the wear properties of the nanocomposites [60, 61].

A continuous improvement in the tribological properties of the Al-hBN nanocomposites was seen with the addition of up to 3 wt.% of hBN in the Al matrix. The larger size of the hBN agglomerates deteriorated the wear resistance of the nanocomposites, and hence during the wear test we see a large amount of wear debris on the wear track, which has been pulled out from the wear track. Agglomeration of the nanofiller in the Al matrix was found to affect the relative density, hardness, and wear properties of the nanocomposites. Pull-out of particles was seen in the SEM image of the wear track of the Ah5 sample in Figures 20(i, j).

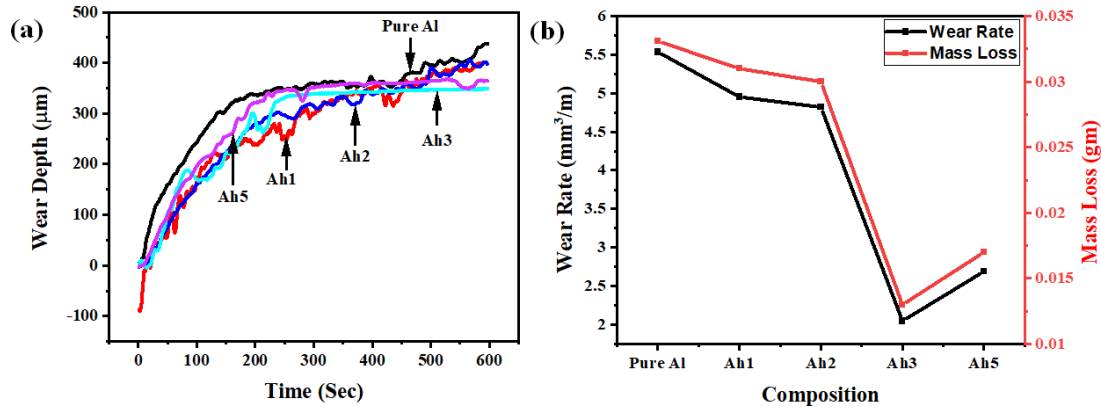From the SEM images of the wear tracks of the

Fig. 19. Variation of (a) wear depth and (b) wear rate and mass loss of sintered pure Al and various Al-hBN nanocomposites
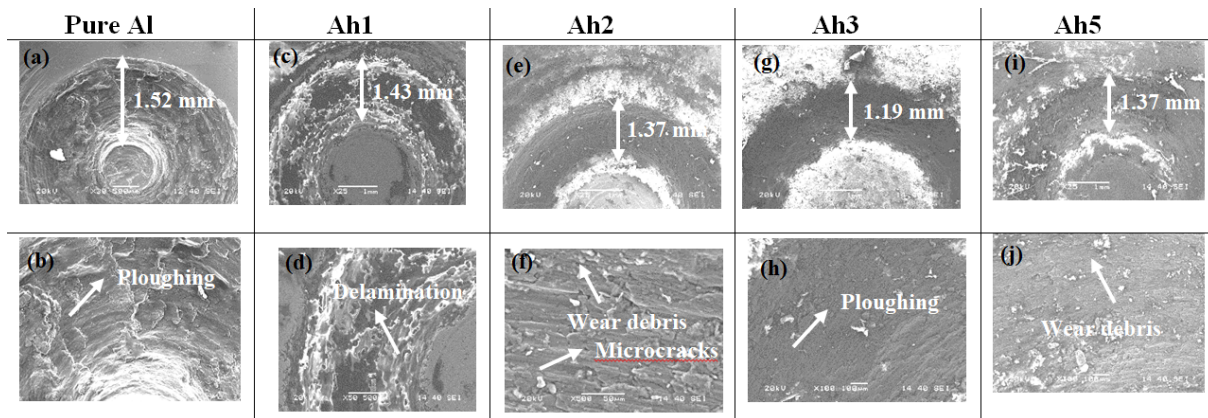

Fig. 20. SEM images of the wear tracks of sintered pure Al and various Al-hBN nanocomposites

sintered pure Al sample and the various Al-hBN nanocomposites in Figure 20, it is evident that the width of the wear track decreases up to the addition of 3 wt.% hBN nanofiller in the Al matrix. The width of the wear track is lowest in the case of the Ah3 nanocomposite, having been found to be ~1.19 mm. The wear track of the Ah3 samples was found to show the least number of cracks and delaminations.

Figure 19(a) also shows that the Ah3 sample had the least wear depth and provided the highest wear resistance. Figure 19(b) also confirms that the Ah3 sample showed the least wear rate as well as mass loss during the wear test. Uniform dispersion of the hBN nanofiller in the Al matrix results in significant improvement in the wear resistance on the Al-hBN nanocomposites. Deep grooves can be

seen in the wear track of the Ah2 sample in Figures 20(e, f). Cracks and delaminations can be seen in the SEM image of the wear track of the pure Al sample in Figures 20(a, b). Ploughing and delaminations can be seen in the SEM image of the wear track of the Ah1 sample in Figures 20(c, d). Due to the pull-out of the particles, wear debris can also be seen in the wear track of the Ah5 sample in Figures 20(i, j).

The compression test is a highly effective mechanical test that is done to understand a material's response under continuous applied load. In a compression test, a compressive load is applied applying a uniaxial force on a stationary sample. After measuring the initial gauge dimension of the sample specimen, the flat sample is placed at the center between the upper and lower anvils. The test
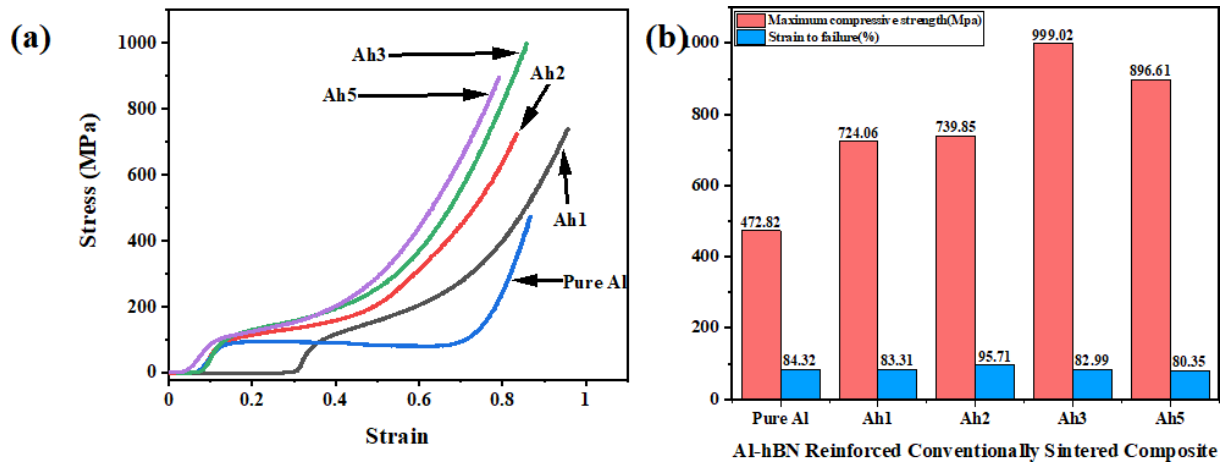
Fig. 21. (a) σ-ε curves of pure Al and the various hBN reinforced nanocomposites, (b) comparison of compressive strength (σ_{max}) and strain to failure (ε_f)

Table 1. A comparative analysis of the properties of the Al-hBN nanocomposites achieved in the present study and by other researchers

Composition	Hardness (MPa)	Relative Density (%)	Sintered Density (g/cc)	Wear rate (mm³/m)	Method	References
Al-3 wt.% hBN	450	94.11	2.52	2.048 (at 15N load)	PM route and conventional sintering	Present Study
Al-3 wt.% hBN	108 HV$_{0.2}$ for BN micro particle (BNMP) and 103 HV$_{0.2}$ for BN nanoparticle (BNNP)	>97	2.675		PM route and spark plasma sintering (SPS)	[16]
Al-3, 6, 9, 12, 15 wt.% hBN	418.3 (for 12 wt.% hBN)	–	2.975 (for 3 wt.% hBN)	–	PM route	[18]
AA2024-7.5 wt.% hBN	1078	–	–	0.002 (at 10N load)	PM route	[19]
AA7150-hBN	1767 (for 1.5 wt.% hBN)	99.82	2.81 (for 1.5 wt.% hBN)	–	Ultrasonic vibration assisted double stir casting process	[65]

is stopped when a crack is initiated on the sample. The data obtained from the Universal Testing Machine (UTM) was used to plot the force-displacement curves of the various samples using a computer. The obtained data was converted to σ-ε data, and from the σ-ε profile the modulus (E), ultimate compressive stress (σ_{max}), and strain to failure (ε_f) were determined. Against the applied load in a single axis, the sample underwent a change in the axial and transverse direction and instant change in size was continuously recorded and plotted in the σ-ε profile.

The compressive tests were carried out using an Instron 8862 UTM with a loading capacity of up to 100 kN. After placing the sample between the compression anvils, the load was increased gradually at a constant strain rate of 0.5 mm/min. Figure 21(a) shows the σ-ε plot of the conventionally
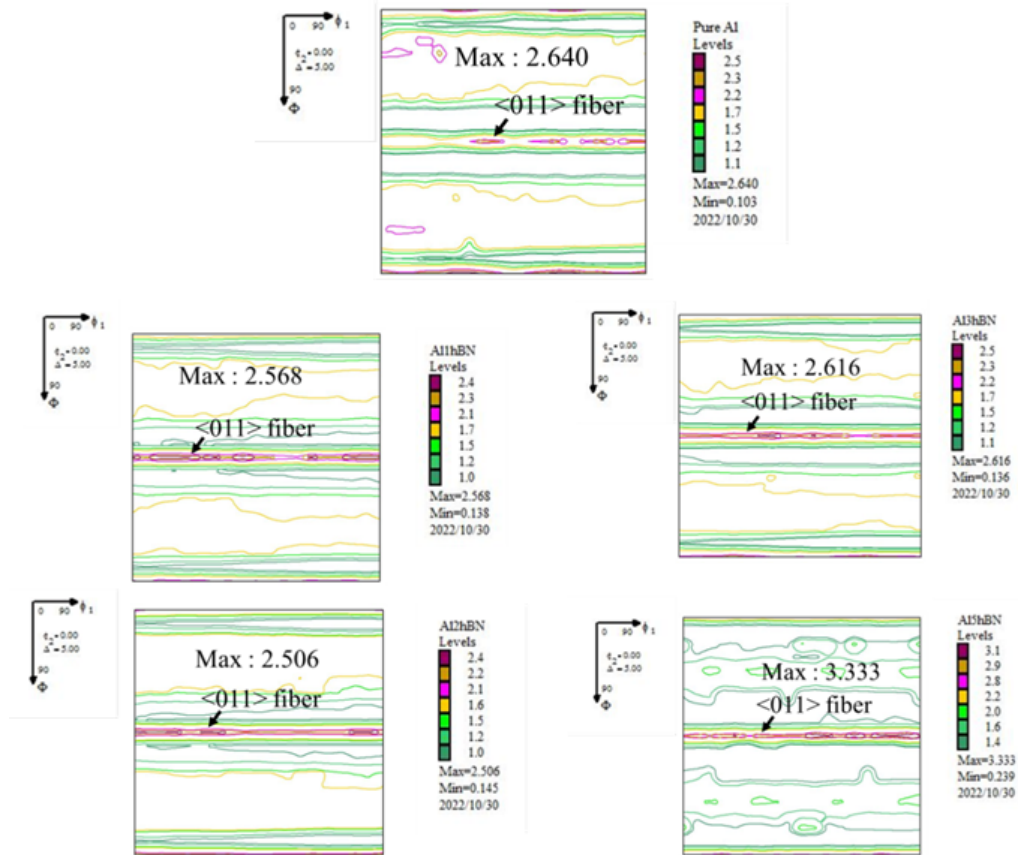
Fig. 22. ODF maps (at constant $\phi 2 = 0°$) of (a) sintered pure Al, (b) Al-1 wt.% hBN, (c) Al-2 wt.% hBN, (d) Al-3 wt.% hBN composites, and (e) Al-5 wt.% hBN nanocomposite

sintered pure Al sample and the various Al-hBN nanocomposites. The compression tests were carried out until the initiation of a crack in the samples [62, 63]. From the σ-ε plots the maximum compressive strength (σ_{max}) and the strain to failure (ε_f) of the samples were determined. The Ah3 sample showed the highest compressive strength (σ_{max}) of ~999.02 MPa, while the lowest compressive strength (σ_{max}) was observed in the case of the pure Al (Ah0) sample (~472.82 MPa). The highest strain to failure (ε_f) was observed in the case of Ah2 nanocomposite (~95.71%) and the lowest strain to failure (ε_f) was observed in the case of Ah5 (80.35). More precisely, the compressive strength (σ_{max}) of the Ah3 sample was more than twice that of the pure Al sample (Ah0), and a decrease in its strain to failure (ε_f) of ~1.6% was also observed compared to the pure Al (Ah0) sample

developed similarly. Therefore, an increase in the compressive strength of the Ah3 sample was accompanied by a reduction in its ductility as compared to the pure Al sample.

The decrease in the σ_{max} value of the Ah5 sample can be attributed to the agglomeration of the hBN nanoreinforcement when its loading level was increased beyond 3 wt.%. Agglomerates of the hBN nanofiller were seen in the SEM micrograph of the Ah5 sample in Figure 15(g) and its elemental map in Figure 15(h). Agglomeration of the nanofiller in the Al matrix resulted in the degradation of the compressive strength of the nanocomposites. Nonuniform densification of the fabricated samples was observed in the case of the Al-hBN nanocomposites having higher weight fraction of hBN [64]. Apart from the compressive strength agglomeration of hBN, nanofiller also diminished the

relative density, hardness, and wear properties of the nanocomposites.

Figure 22 shows the orientation distribution function (ODF) developed at constant $\varphi_2 = 0°$ for pure Al and Al-hBN nanocomposites developed by conventional sintering as a function of loading level of the hBN reinforcement. It was observed that the $<011>$ fiber is the dominant fiber in the pure Al sample [66, 67], and that the $<011>$ fiber had been strengthened after addition of the hBN nanoreinforcement in the Al matrix. A dominant $<011>$ fiber texture was observed for the pure Al, as well as all the various Al-hBN nanocomposites. The maximum intensities of the $<011>$ fiber in pure Al and Al-1, 2, 3, and 5 wt.% hBN were 2.64, 2.56, 2.50, 2.61, and 3.33, respectively. It can be seen that there have not been many changes in the intensity of the $<011>$ fiber with the addition of the hBN. Only a slight increase in the $<011>$ fiber volume fraction was observed up to the addition of 5 wt.% of hBN in the Al matrix. The Al-5 wt.% hBN showed the highest intensity of the $<011>$ fiber.

This variation in the texture can be correlated with trends in other mechanical proprieties observed in Al-hBN nanocomposites. There has been a significant effect on the hardness and wear of the Al-hBN nanocomposites due to the addition of the hBN nanofiller in the Al matrix, and the highest hardness and wear has been observed in the case of Al-3 wt.% hBN nanocomposite. A homogenous distribution of the nanofiller in the Al matrix resulted in significant improvement of the hardness as well as the wear properties. However, increasing the hBN loading level beyond 3 wt.% resulted in the deterioration of the mechanical and wear properties of the Al-hBN nanocomposites due to agglomeration of the hBN nanofiller in the Al matrix. From texture analysis, it has been justified that a random texture with $<011>$ fibers is present in the nanocomposites.

4. Conclusions

Hexagonal boron nitride (hBN) powder was milled in a planetary ball mill at 300 rpm for up to 30 hours. The objective of the present research work was to find out the effect of milling time on the structure and morphology of the hBN. The as-received pristine hBN was then added to the Al matrix to develop Al-1, 2, 3, and 5 wt.% hBN nanocomposites by powder metallurgy (PM). The following conclusions were drawn from the present work.

1. The crystallite size of hBN after 20 hours of milling was calculated using the Voigt's formula and was found to be 18 nm. The nanostructured nature of the 20-hour-milled hBN was also confirmed by the HRTEM analysis.

2. Milling resulted in the exfoliation of the hBN platelets, and the 20-hour-milled hBN powder showed few layers of hBN stacked together. The hBN layers were electron transparent, and a few hBN films with folded edges could also be seen in the HRTEM images.

3. Among the various Al-hBN nanocomposites developed by PM route, Al-3 wt.% hBN nanocomposite showed the highest relative density. The Al-3 wt.% hBN nanocomposite also showed the highest hardness (450 MPa) and wear resistance. A 40% improvement in hardness as compared to pure Al sample developed similarly was observed in the case of the Al-3 wt.% hBN nanocomposite. The Al-3 wt.% hBN nanocomposite also showed the highest compressive strength of of ~999 MPa. The addition of hBN beyond 3 wt.% in the Al matrix resulted in deterioration of densification of the nanocomposites and also lower hardness and poorer wear resistance in the nanocomposite. Al-3 wt.% hBN nanocomposite (Ah3) exhibited the maximum relative density of 94.11% among all the Al-hBN nanocomposites and the pure Al sample that was developed similarly. The loading level of 3 wt.% hBN was found to be the optimum loading level of the nanofiller, which resulted in the best physical and mechanical properties of the Al-hBN nanocomposite.

4. Proper dispersion of the hBN nanofiller in the Al metal matrix, which was achieved

at lower loading levels of up to 3 wt.% in the hBN nanofiller,was highly effective in enhancing the mechanical properties of the Al-hBN nanocomposites. A continuous increase in relative density, hardness and wear resistance was observed up to the loading level of 3 wt.% of hBN. Addition of hBN larger than this amount in the Al matrix resulted in the agglomeration of the nanofiller in the Al matrix, which resulted in deterioration of the relative density hardness and the wear properties of the nanocomposite.

Acknowledgements

Conflict of interest

The authors declare that they have no known competing financial interests or personal relationships that could have appeared to influence the work reported in this paper.

References

[1] Kumar HGP, Xavior MA. Graphene reinforced metal matrix composite (GRMMC): a review. Procedia Eng. 2014;97:1033–40.

[2] Srivastava AK, Sharma B, Saju BR, Shukla A, Saxena A, Maurya NK. Effect of graphene nanoparticles on microstructural and mechanical properties of aluminum based nanocomposites fabricated by stir casting. World J Eng. 2020;17(6): 859–866.

[3] Li Y, Zhao YH, Ortalan V, Liu W, Zhang ZH, Vogt RG et al. Investigation of aluminum-based nanocomposites with ultra-high strength. Mater Sci Eng: A. 2009;527(1–2):305–16.

[4] Oku T, Hirano T, Kuno M, Kusunose T, Niihara K, Suganuma K. Synthesis, atomic structures and properties of carbon and boron nitride fullerene materials. Mater Sci Eng B: Adv Funct Solid-State Mater. 2000;74(1):206–17.

[5] Sharker SM. Hexagonal boron nitrides (white graphene): a promising method for cancer drug delivery. Int J Nanomed. 2019;14:9983–93.

[6] Yankowitz M, Ma Q, Jarillo-Herrero P, LeRoy BJ. Van der Waals heterostructures combining graphene and hexagonal boron nitride. Nat Rev Phys. 2019;1(2):112–25.

[7] Wang J, Ma F, Sun M. Graphene, hexagonal boron nitride, and their heterostructures: properties and applications. RSC Adv. 2017;7(27):16801–22.

[8] Ertug B. Powder preparation, properties and industrial applications of hexagonal boron nitride, in sintering applications. InTech. 2013.

[9] Bhimanapati GR, Glavin NR, Robinson JA. 2D boron nitride: synthesis and applications. *Semicond Semimet.* 2016;95:101–47.

[10] Topsakal M, Aktürk E, Ciraci S. First-principles study of two- and one-dimensional honeycomb structures of boron nitride. Phys Rev. B. 2009;79(11):115442.

[11] Peng Q, Ji W, De S. Mechanical properties of the hexagonal boron nitride monolayer: Ab initio study. Comput Mater Sci. 2012;56:11–17.

[12] Golberg D, Bando Y, Huang Y, Terao T, Mitome M, Tang C, Zhi C. Boron nitride nanotubes and nanosheets. ACS Nano. 2010;4(6):2979–93.

[13] Leng C, Hu X, Xie H, Shen C. Thermal properties of polycrystalline cubic boron nitride sintered under high pressure condition. Sci Sinter. 2018;50(4):401–8.

[14] Falin A, Cai Q, Santos EJG, Scullion D, Qian D, Zhang R, Yang Z, et al. Mechanical properties of atomically thin boron nitride and the role of interlayer interactions. Nat Commun. 2017;8:15815.

[15] Silicka MJ, Trukawka M, Piotrowska K, Mijowska E. Few-layered hexagonal boron nitride: functionalization, nanocomposites, and physicochemical and biological properties. In: Ince M, Ince OK, Ondrasek G, editors. Biochemical toxicology—heavy metals and nanomaterials. London: IntechOpen; 2020. p. 155–71.

[16] Firestein KL, Corthay S, Steinman AE, Matveev AT, Kovalskii AM, Sukhorukova IV, et al. High-strength aluminum-based composites reinforced with BN, AlB2 and AlN particles fabricated via reactive spark plasma sintering of Al-BN powder mixtures. Mater Sci Eng: A. 2017;681:1–9.

[17] Khatavkar RA, Mandave AK, Baviskar DD, Shinde SL. Influence of hexagonal boron nitride on tribological properties of AA2024-hBN metal matrix composite. Int Res J Eng Technol. 2018;5(5):3792–8.

[18] Yonetken A, Erol A. Production and characterization of Al-BN composite materials using by powder metallurgy. Agron Res. 2018;16(S1):1289–94.

[19] Loganathan P, Gnanavelbabu A, Rajkumar K. Investigation on mechanical and wear behaviour of AA2024/hBN composites synthesized via powder metallurgy routine. Mater Today: Proc. 2021;45(9):7865–70.

[20] Gostariani R, Ebrahimi R, Asadabad MA, Paydar MH. Mechanical properties of Al/BN nanocomposites fabricated by planetary ball milling and conventional hot extrusion. Acta Metall Sin. (English Letters). 2018;31(3):245–53.

[21] Gautam C, Chelliah S. Methods of hexagonal boron nitride exfoliation and its functionalization: covalent and non-covalent approaches. RSC Adv. 2021;11:31284–327.

[22] Huang J, E Songfeng, Li J, Jia F, Ma Q, Hua L, Lu Z. Ball-milling exfoliation of hexagonal boron nitride in viscous hydroxyethyl cellulose for producing nanosheet films as thermal interface materials. ACS Appl Nano Mater. 2021;4(12):13167–75.

[23] Langford JI. Accuracy in powder diffraction. In: NBS

Special Publication No. 567. Block S, Hubbard CR, editors. 567:255–69.

[24] Alam SN. Synthesis and characterization of W-Cu nanocomposites developed by mechanical alloying. Mater Sci Eng: A. 2006;433(1–2):161–8.

[25] Warren BE, Averbach BL. The effect of cold-work distortion on x-ray patterns. J Appl Phys. 1950;21:595–9.

[26] Bachmann F, Hielscher R, Schaeben H. Texture analysis with MTEX-free and open source software toolbox. Solid State Phenom. 2010;60:63–8.

[27] Cullity BD, Stock SR. Elements of x-ray diffraction. Upper Saddle River, New Jersey: Prentice Hall; 2001.

[28] Suryanaryana C, Norton MG. X-ray diffraction: a practical approach. New York: Springer; 1998.

[29] Balzar D, Ledbetter H. Voigt-function modeling in Fourier analysis of size- and strain-broadened x-ray diffraction peaks. J Appl Crystallogr. 1993;26(1):97–103.

[30] Langford JI. A rapid method for analysing the breadths of diffraction and spectral lines using the Voigt function. J Appl Crystallogr. 1978;11:10–14.

[31] de Keijser TH, Langford JI, Mittemeijer EJ, Vogels ABP. Use of Voigt function in a single-line method for the analysis of x-ray diffraction line broadening. J Appl Crystallogr. 1982;15:308–14.

[32] Santra K, Chatterjee P, Sengupta SP. Voigt modelling of size-strain analysis: application to Al2O3 prepared by combustion technique. Bull Mater Sci. 2002;25(3):251–7.

[33] Yu C, Zhang J, Tian W, Fan X, Yao Y. Polymer composites based on hexagonal boron nitride and their application in thermally conductive composites. RSC Adv. 2018;8:21948–67.

[34] Kostoglou N, Polychronopoulou K, Rebholz C. Thermal and chemical stability of hexagonal boron nitride (h-BN) nanoplatelets. Vacuum. 2015;112:42–5.

[35] Kostoglou N, Lukovic J, Babic B, Matovic B, Photiou D, Constantinides G, et al. Few-step synthesis, thermal purification and structural characterization of porous boron nitride nanoplatelets. Mater Des. 2016;110:540–8.

[36] Hou X, Yu Z, Chou KC. Preparation and properties of hexagonal boron nitride fibers used as high temperature membrane filter. Mater Res Bull. 2014;49:39–43.

[37] Cai Q, Scullion D, Falin A, Watanabe K, Taniguchi T, Chen Y, et al. Raman signature and photon dispersion of atomically thin boron nitride. Nanoscale. 2017;9:3059–67.

[38] Stenger I, Schue L, Boukhicha M, Berini B, Placais B, Loiseau A, Barjon J. Low frequency Raman spectroscopy of few-atomic-layer thick hBN crystal. 2D Mater. 2017;4(3):031003.

[39] Yassin OA, Alamri SN, Joraid AA. Effect of particle size and laser power on the Raman spectra of CuAlO2 delafossite nanoparticles. J Phys D: Appl Phys. 2013;46:235301.

[40] Gomez DA, Coello J, Maspoch S. The influence of particle size on the intensity and reproducibility of Raman spectra of compacted samples. Vib Spectrosc. 2019;100:48–56.

[41] Elbadawi C, Tran TT, Kolíbal M, Šikola T, Scott J, Cai Q, et al. Electron beam directed etching of hexagonal boron nitride. Nanoscale. 2016;8:16182.

[42] Jeong H, Kim DY, Kim J, Moon S, Han N, Lee SH et al. Wafer-scale and selective-area growth of high-quality hexagonal boron nitride on Ni(111) by metal-organic chemical vapor deposition. Sci Rep. 2019;9:5736.

[43] Deepika, Li LH, Glushenkov AM, Hait SK, Hodgson P, Chen Y. High-efficient production of boron nitride nanosheets via an optimized ball milling process for lubrication in oil. Sci Rep. 2014;4:7288.

[44] Langhi MP, Isotani S, Chubaci JFD. Fourier transform infrared spectroscopy analysis of thin boron nitride films prepared by ion beam assisted deposition. Phys Status Solidi C: Curr Top Solid State Phys. 2014;11(3–4):509–12.

[45] Gao G, Mathkar A, Martins EP, Galvão DS, Gao D, da Silva Autreto PA, et al. Designing nanoscaled hybrids from atomic layered boron nitride with silver nanoparticle deposition. J Mater Chem A. 2014;9(2):3148–54.

[46] Ahmad P, Khandaker MU, Amin YM, Muhammad N. Synthesis of highly crystalline multilayered boron nitride microflakes. Sci Rep. 2016;6:21403.

[47] Zhang B, Wu Q, Yu H, Bulin C, Sun H, Li R, et al. High-efficient liquid exfoliation of boron nitride nanosheets using aqueous solution of alkanolamine. Nanoscale Res Lett. 2017;12:596.

[48] Shao I, Vereecken PM, Chien CL, Searson PC, Cammarata RC. Synthesis and characterization of particle-reinforced Ni/Al2O3 nanocomposites. J Mater Res. 2002;17(6):1412–8.

[49] Chugh D, Jagadish C, Tan H. Large-area hexagonal boron nitride for surface enhanced Raman spectroscopy. Adv Mater Technol. 2019;4(8):1900220.

[50] Zhang Z, Chen DL. Consideration of Orowan strengthening effect in particulate-reinforced metal matrix nanocomposites: a model for predicting their yield strength. Scr Mater. 2006;54(7):1321–6.

[51] Huo S, Xie L, Xiang J, Pang S, Hu F, Umer U. Atomic-level study on mechanical properties and strengthening mechanism of Al/SiC nano-composites. Appl Phys A. 2018;124:209.

[52] Mattli MR, Matli PR, Khan A, Abdelatty RH, Yusuf M, Al Ashraf A, et al. Study of microstructural and mechanical properties of al/sic/tio2 hybrid nanocomposites developed by microwave sintering. Crystals. 2021;11:1078.

[53] Zare Y, Rhee KY, Hui D. Influences of nanoparticles aggregation/agglomeration on the interfacial/interphase and tensile properties of nanocomposites. Compos B: Eng. 2017;122:41–6.

[54] Krishnan P, Lakshmanan P, Palani S, Arumugam A, Kulothungan S. Analyzing the hardness and wear properties of SiC and hBN reinforced aluminum hybrid nanocomposites. Mater Today Proc. 2022;62(2):566–71.

[55] Shu R, Jiang X, Liu W, Shao Z, Song T, Luod Z. Synergetic effect of nano-carbon and HBN on microstructure and mechanical properties of Cu/Ti3SiC2/C nanocomposite. Mater Sci Eng: A. 2019;755:128–37.

[56] Kelly A, Nicholson RB, Editors. Strengthening methods in crystals. Amsterdam: Elsevier; 1971.

[57] Huo S, Xie L, Xiang J, Pang S, Hu F, Umer U. Atomic-level study on mechanical properties and strengthening mechanisms of Al/SiC nano-composites. Appl Phys A. 2018;124:209.

[58] Kumar S, Kumar A, Poddar A, Asthana P. Investigation on wear behavior of aluminium matrix micro and nanocomposites. Mater Today Proc. 2022;56(5):2839–45.

[59] Hemanth G, Suresha B, Hemanth R. The effect of hexagonal boron nitride on wear resistance under two and three-body abrasion modes of polyetherketone composites. Surf Topogr: Metrol Prop. 2019;7(4):045019.

[60] Panda N, Bijwe J, Pandey RK. Role of micro and nanoparticles of hBN as a secondary solid lubricant for improving tribo-potential of PEAK composite. Tribol Int. 2019;30:400–12.

[61] Chin J, Chen B, Li J, Tong X, Zhao H, Wang L. Enhancement of mechanical and wear properties performance in hexagonal boron nitride-reinforced epoxy nanocomposites. Polym Int. 2017;66(5):659–64.

[62] Şenel MC, Gürbüz M. Synergistic effect of graphene/boron nitride binary nanoparticles on aluminum hybrid composite properties. Adv Compos Hybrid Mater. 2021;4:1248–60.

[63] Nayak B, Sahu RK, Karthikeyan P. Study of the tensile and compressive behaviour of the in-house synthesized Al-alloy nanocomposite. In: 2nd International Conference on Advances in Mechanical Engineering (ICAME 2018), IOP Conf Ser: Mater Sci Eng. 2018;402:012070.

[64] Zare Y. Study of nanoparticles aggregation/agglomeration in polymer particulate nanocomposites by mechanical properties. Compo A: Appl Sci Manuf. 2016;84:158–64.

[65] Madhukar P, Selvaraj N, Rao CSP, Kumar GBV. Fabrication and characterization two-step stir casting with ultrasonic assisted novel AA7150-hBN nanocomposites. J Alloys Compd. 2020;815:152464.

[66] Haouaoui M, Hartwig KT, Payzant EA. Effect of strain path on texture and annealing Mmicrostructure development in bulk pure copper processed by simple shear. Acta Mater. 2005;53:801–10.

[67] Paul H, Maurice C, Driver JH. Microstructure and microtexture evolution during strain path changes of an initially stable cu single crystal. Acta Mater. 2010;58:2799–813.